Check for updates

Synergistic redox enhancement: silver phosphate augmentation for optimizing magnesium copper phosphate in efficient energy storage devices and oxygen evolution reaction†

Haseebul Hassan,[a] Muhammad Waqas Iqbal, [ID] *[a] Nora Hamad Al-Shaalan, [ID] [b] Sarah Alharthi, [ID] [c] Nawal D. Alqarni,[d] Mohammed A. Amin[c] and Amir Muhammad Afzal[a]

The implementation of battery-like electrode materials with complicated hollow structures, large surface areas, and excellent redox properties is an attractive strategy to improve the performance of hybrid supercapacitors. The efficiency of a supercapattery is determined by its energy density, rate capabilities, and electrode reliability. In this study, a magnesium copper phosphate nanocomposite ($MgCuPO_4$) was synthesized using a hydrothermal technique, and silver phosphate (Ag_3PO_4) was decorated on its surface using a sonochemical technique. Morphological analyses demonstrated that Ag_3PO_4 was closely bound to the surface of amorphous $MgCuPO_4$. The $MgCuPO_4$ nanocomposite electrode showed a 1138 C g^{-1} capacity at 2 A g^{-1} with considerably improved capacity retention of 59% at 3.2 A g^{-1}. The increased capacity retention was due to the fast movement of electrons and the presence of an excess of active sites for the diffusion of ions from the porous Ag_3PO_4 surface. The $MgCuPO_4$–Ag_3PO_4//AC supercapattery showed 49.4 W h kg^{-1} energy density at 550 W kg^{-1} power density and outstanding capacity retention (92% after 5000 cycles). The experimental findings for the oxygen evolution reaction reveal that the initial increase in potential required for $MgCuPO_4$–Ag_3PO_4 is 142 mV, indicating a clear Tafel slope of 49 mV dec^{-1}.

1. Introduction

Nowadays, the most commonly used energy resources are fossil fuels, which lead to the emission of hazardous gases into the environment. Moreover, the increasing demand for energy is resulting in the quick depletion of these energy resources. All of these circumstances require renewable energy resources to fulfill energy requirements. However, due to the intermittent behavior of wind and solar energy resources, the use of energy storage devices (ESDs) has become more prominent. An ESD balances the demands and supply of electricity. Two similar kinds of electrode are used in electric double-layer capacitors (EDLCs) that deliver quick bursts of energy, long cycle life, and

exceptional power density. However, they have low energy density, limiting their ability to meet increasing technological needs.[1,2] Lithium-ion batteries have high energy but have a disadvantage in delivering quick bursts of energy, which significantly lowers their life span compared to an EDLC. Furthermore, if overloaded or overheated, an LIB can explode.[3,4] There have been numerous efforts to broaden the EDLC working potential and increase its energy while maintaining its power density. A new asymmetric device known as a supercapattery has recently received a lot of attention because it combines capacitive-graded materials (electrostatic storage) and other battery-graded materials (faradaic storage). RuO_2, a well-known outstanding pseudocapacitor electrode, demonstrated an exceptional capacitance of 1340 F g^{-1}. But its high expense and ecotoxicity prevent it from being used commercially. Other oxide-based metals, such as NiO and Co_3O_4, show promise, but their electrical resistance is low. As a result, it is critical to identify materials for a supercapattery that are inexpensive but have similar effectiveness to current materials.[5,6] The catalysts used in the oxygen electrode for the oxygen evolution reaction (OER) have garnered significant attention due to their crucial role in these systems. There is an urgent need to develop highly efficient catalysts, free of noble metals,

[a]Department of Physics, Riphah International University, Campus Lahore, Pakistan. E-mail: waqas.iqbal@riphah.edu.pk

[b]Department of Chemistry, College of Science, Princess Nourah Bint Abdulrahman University, P. O. Box 84428, Riyadh 11671, Saudi Arabia

[c]Department of Chemistry, College of Science, Taif University, P. O. Box 11099, Taif, Saudi Arabia

[d]Department of Chemistry, College of Science, University of Bisha, Bisha, 61922, Saudi Arabia

that exhibit superior catalytic activity for the OER. This need arises from the desire to replace expensive and scarce RuO_2 and IrO_2 catalysts.[7]

Scientists are presently focusing on tertiary phosphides as encouraging electrodes in supercapacitors. For example, Lei *et al.*[8] used a simple hydrothermal process to make a ZnNiCoP–NF nanostructure, which showed 1111 C g^{-1} capacity at 10 A g^{-1}. They demonstrated that the fabricated electrochemical design is ideal for energy-storage uses. Yang *et al.*[9] produced Ni–Co–Mo ternary phosphide formed on carbon cloth fibers, which had a specific capacitance of 433 F g^{-1} at 1 A g^{-1} current density.

Silver is undoubtedly a viable substitute for carbon-based materials. Moon *et al.*[10] developed a translucent and flexible supercapacitor with silver nanowires coated with gold. Despite their widespread use in bendable and wearable electrical devices, silver nanowire networks have high contact resistance among the nanowires.[11–13] Silver nanoparticles with graphene, metal oxides, carbon nanotubes, and conducting polymers were tried earlier. A matrix of Ag with carbon in a composite form shows no pseudocapacitance. However, due to the increased electrical activity, its EDLC performance improves. The Ag/PANI nanocomposite synthesized by Patil *et al.*[14] and Tang *et al.*[15] showed that the presence of Ag in a PANI heterostructure makes the movement of ions faster. The Ag coating on PANI produces high specific energy due to quicker electron transport and electrolyte access *via* a porous network.[16] Copper phosphate (Cu_2PO_4) is thought to be a perfect alternative to conventional metallic phosphates since Cu has significantly greater conductance. Cu_2PO_4 exhibits further intriguing dielectric and thermal characteristics. The efficacy of Cu_2PO_4 in supercapacitors has received little attention. Its electrochemical performance was improved by incorporating metal ions, which increases the conductivity. Thus, additional attempts to enhance the electrical conductivity of such electrode materials are required. The addition of another metal ion with similar properties can significantly improve the electrical characteristics. Thus, the movement of ions between the two metal phosphates becomes easier and the interfacial impedance of the composite substance can be reduced. Additionally, a large useful surface area is accessible for a redox reaction, increasing the capacity and power density of the supercapacitor.[17]

Herein, precipitation followed by calcination was used to produce silver phosphate nanoparticles (Ag_3PO_4 NPs) on amorphous $MgCuPO_4$. Because of its high electrical conductivity, Ag was selected to improve the electrical conductivity of amorphous $MgCuPO_4$. To prevent the recombination of particles, an amorphous $MgCuPO_4$ and silver complex ($Ag(NH_3)_2^+$) mixture was made using a sonochemical technique. $MgCuPO_4$–Ag_3PO_4 composites were developed to raise the energy density, reduce resistance, and expand the supercapattery cycle life. The presence of low-E_g metal ions in the amorphous structure of $MgCuPO_4$ is still a novel way to increase the supercapacitive performance. Furthermore, the application of the oxygen evolution reaction (OER) was also examined in the context of $MgCuPO_4$–Ag_3PO_4 composites. The impact of different $MgCuPO_4$ to Ag_3PO_4 weight ratios on the overall storage

capability was investigated. A comprehensive charge transfer procedure between $MgCuPO_4$ and solid Ag_3PO_4 was observed.

2. Experimental work

2.1. Materials

Carbon black, magnesium nitrate hexahydrate ($Mg(NO_3)_2 \cdot 6H_2O$), hydrochloric acid (HCl), copper(II) nitrate tri-hydrate ($Cu(NO_3)_2 \cdot 3H_2O$), NMP, and silver nitrate ($AgNO_3$) were received from Friendemann Schmidt. Tri-sodium phosphate (Na_3PO_4) and potassium hydroxide pellets (KOH) were bought from Duksan Pure Chemicals. All of the materials used were of analytical quality and were used without purification. Deionized water (DIW) was used throughout the experiments.

2.2. Synthesis of $MgCuPO_4$–Ag_3PO_4

A hydrothermal and sonochemical technique was used to synthesize $MgCuPO_4$–Ag_3PO_4 composites with various weight ratios of $MgCuPO_4$ and Ag_3PO_4. The as-prepared $MgCuPO_4$ (set A) was made using the methods described in the literature.[18] First, 0.8 M magnesium nitrate hexahydrate ($Mg(NO_3)_2 \cdot 6H_2O$) solution was mixed with a 0.8 M solution of copper(II) nitrate trihydrate ($Cu(NO_3)_2 \cdot 3H_2O$). The mixture was stirred continuously for 25 min and transferred into an autoclave and heated at 140 °C. The centrifuge machine (10 000 rpm Model RST-10M) was used to eliminate impurities from the solution. After drying at 40 °C the prepared $MgCuPO_4$ was collected. The addition of NH_3 into a 0.5 M solution of $AgNO_3$ reduces Ag^+. A horn sonicator was used for sonication until a diaminesilver(I) complex was produced. The complex solution of diaminesilver(I) was then combined with 0.02 g of $MgCuPO_4$ solution and continuously stirred (3–4 h). The mixture was rinsed many times with DIW before drying for 4 h at 40 °C. Finally, the desiccated materials were calcined for 3 h at 300 °C and labeled S_1. Two more $MgCuPO_4$–Ag_3PO_4 nanocomposites were made for optimization reasons by altering the wt% ratio of as-prepared $MgCuPO_4$ to 0.03 and 0.05 g and they were designated S_2 and S_3, respectively. Fig. 1 shows the synthetic process for $MgCuPO_4$–Ag_3PO_4 nanocomposites. Table 1 shows different wt% ratios in three different composites of $MgCuPO_4$–Ag_3PO_4 (S_1, S_2, and S_3).

2.3. Characterization

2.3.1. Structural and surface analysis. The crystalline phases of the materials ($MgCuPO_4$, S_1, S_2, and S_3) were analyzed using XRD (D5000, Siemens). Kα radiation with 1.54 Å wavelength and 0.02 s^{-1} scan rate was used to determine the crystallinity of S_1, S_2, and S_3. FTIR (Thermo Scientific Nicolet IS10 Smart ITR) was used to investigate the purity of the samples (S_1, S_2, and S_3) which were scanned at 1 cm^{-1} resolution. X-ray photoelectron spectroscopy (XPS) measurements were taken at binding energies from 0 to 1000 eV, with 1 eV resolution. Single XPS spectra were performed at a resolution of 0.1 eV. Origin Pro 8.1 was used to fit the spectra with numerous Gaussian curves. Scanning electron microscopy (SEM) was applied to analyze the morphological characteristics of the $MgCuPO_4$–Ag_3PO_4
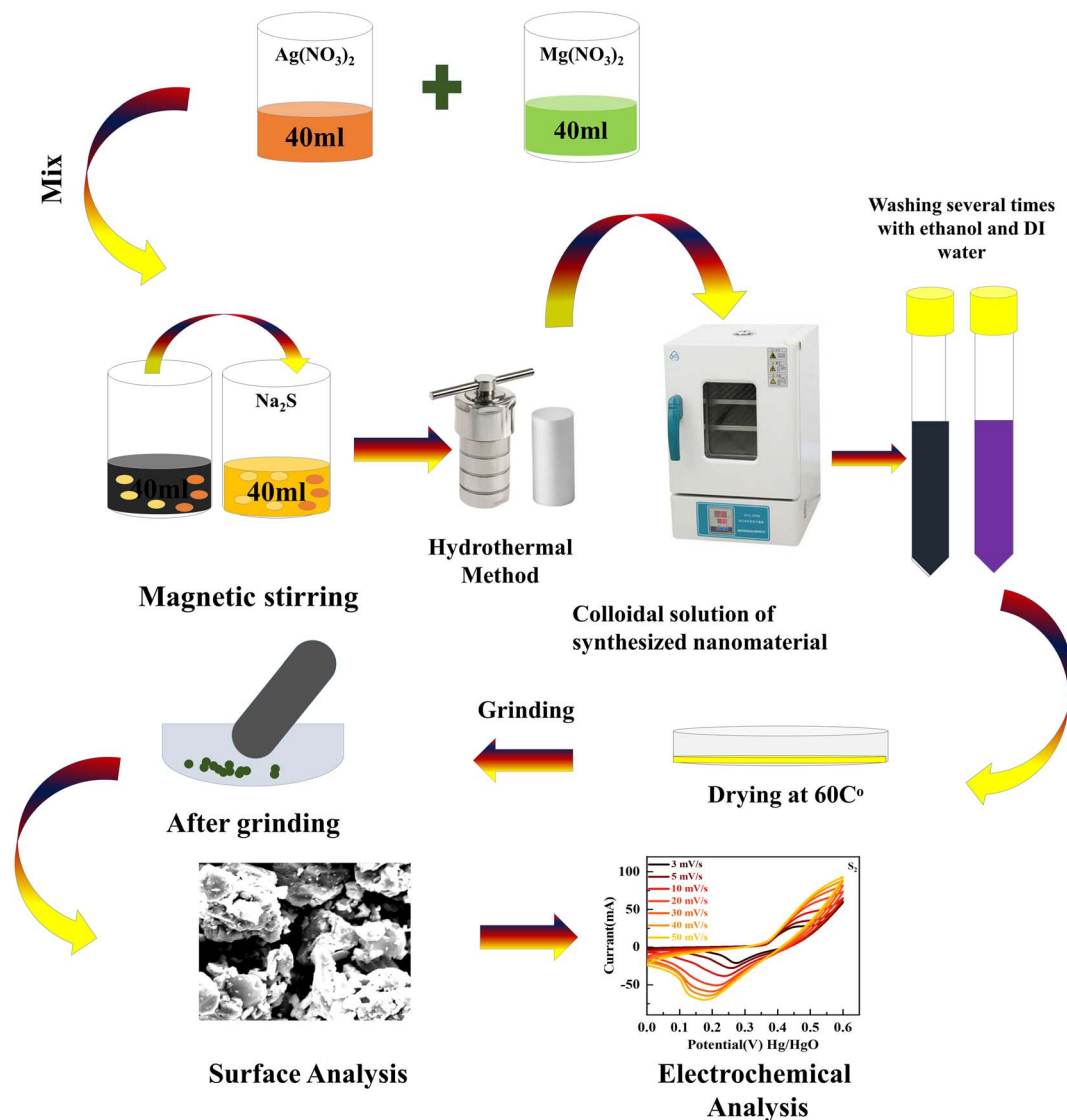
Fig. 1 Systematic illustration of the hydrothermal technique to synthesize MgCuPO$_4$–Ag$_3$PO$_4$ nanocomposites.

Table 1 Different weight ratios of Ag to MgCuPO$_4$ for the synthesis of MgCuPO$_4$–Ag$_3$PO$_4$ nanocomposites

Sample	MgCuPO$_4$ mass	Ag mass	Weight ratio (%)
S$_1$	20 mg	0.4 mg	0.083 : 1
S$_2$	30 mg	0.4 mg	0.145 : 1
S$_3$	50 mg	0.4 mg	0.232 : 1

nanocomposites. Jenway's 6800 design was used to determine the optical absorbance characteristics over a spectral range of 200 to 800 nm.

2.3.2. Electrochemical studies. The active materials (S$_1$, S$_2$, and S$_3$) were coated onto nickel foam (NF) and employed as a working electrode in an electrochemical research setup. In a three-cell setup, the counter and reference electrodes were platinum wire and Hg/HgO, respectively. Throughout the electrochemical studies in a typical cell, a 1 M potassium hydroxide (KOH) solution was kept constant. The slurry for the working electrode was prepared by blending 75% active material (MgCuPO$_4$–Ag$_3$PO$_4$) and 15% carbon black, which were bonded together with the help of PVDF binder (10%). This slurry was mixed continuously for 5–6 h to produce a homogeneous suspension. This suspension was then easily applied to NF. Before starting the experiment, the NF was thoroughly cleaned with HCl, ethanol, acetone, and DIW. The NMP slurry was coated on a 1 × 1 cm^2 area of NF. The total weight of the active material was roughly 5.5 mg. Furthermore, in the supercapattery application, activated carbon (AC) and the best composite were used as the positive and negative electrodes. The electrochemical properties of all of the materials were studied using a workstation CS300 potentiostat. A multi-channel Autolab, PGSTAT30 potentiostat was used for the Mott–Schottky (MS) measurements.
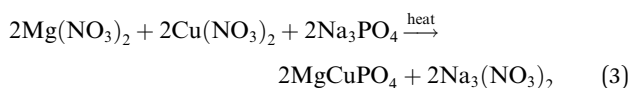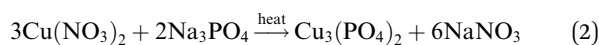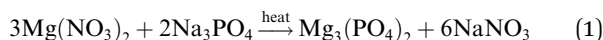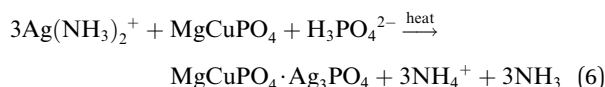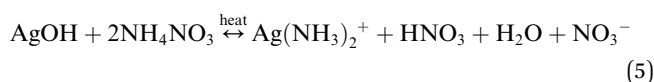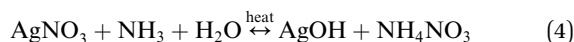
3. Results and discussion

3.1. Characterization of materials

3.1.1. Mechanism of MgCuPO$_4$–Ag$_3$PO$_4$ composite formation.
The equations below were used to describe the formation mechanism of the MgCuPO$_4$–Ag$_3$PO$_4$ nanocomposite. In the first part, a homogeneous suspension of MgCuPO$_4$ nanocomposite was formed using a hydrothermal approach. After that positive Ag(NH$_3$)$_2^+$ was electrostatically bound with the phosphate group and arranged around MgCuPO$_4$. The presence of an excess amount of H$_3$PO$_4^{2-}$ in the as-synthesized MgCuPO$_4$ causes the quick development of a homogeneous MgCuPO$_4$–Ag$_3$PO$_4$ nanocomposite after stirring. Ammonium (NH$_4^+$) and other unwanted impurities were eliminated upon calcination.

MgCuPO$_4$ formation

$$3Mg(NO_3)_2 + 2Na_3PO_4 \xrightarrow{heat} Mg_3(PO_4)_2 + 6NaNO_3 \quad (1)$$

$$3Cu(NO_3)_2 + 2Na_3PO_4 \xrightarrow{heat} Cu_3(PO_4)_2 + 6NaNO_3 \quad (2)$$

$$2Mg(NO_3)_2 + 2Cu(NO_3)_2 + 2Na_3PO_4 \xrightarrow{heat}$$
$$2MgCuPO_4 + 2Na_3(NO_3)_2 \quad (3)$$

MgCuPO$_4$–Ag$_3$PO$_4$ formation

$$AgNO_3 + NH_3 + H_2O \overset{heat}{\leftrightarrow} AgOH + NH_4NO_3 \quad (4)$$

$$AgOH + 2NH_4NO_3 \overset{heat}{\leftrightarrow} Ag(NH_3)_2^+ + HNO_3 + H_2O + NO_3^- \quad (5)$$

$$3Ag(NH_3)_2^+ + MgCuPO_4 + H_3PO_4^{2-} \xrightarrow{heat}$$
$$MgCuPO_4 \cdot Ag_3PO_4 + 3NH_4^+ + 3NH_3 \quad (6)$$

3.1.2. Structural analysis of MgCuPO$_4$–AgPO$_4$.
The crystallinities of MgCuPO$_4$, S$_1$, S$_2$, and S$_3$ were studied by XRD and the outputs are depicted in Fig. 2. First, the XRD of MgCuPO$_4$ was studied, as indicated by Fig. 2(a). There were three different XRD patterns represented by three different colors assigned to Mg$_3$(PO$_4$)$_2$, Cu$_3$(PO$_4$)$_2$, and MgCuPO$_4$. The diffraction spikes at $2\theta = 12°$, $22°$, $23.2°$, $26°$, $28.32°$, $31.3°$, $36.5°$, $38°$, $48.23°$, $52.8°$, and $57.1°$ belong to the (110), (101), (−111), (210), (021), (121), (−221), (031), (330), (−331), and (150) planes, which match JCPDS 33-0876.[19] The XRD peaks for Cu$_3$(PO$_4$)$_2$ showed diffraction spikes at $2\theta = 15.32°$, $21.2°$, $25°$, $31.33°$, $35°$, $37°$, $40°$, $44.3°$, and $56.5°$ belonging to (001), (110), (−101), (001), (121), (210), (200), (013), and (−221), which matches JCPDS 01-080-0991.[20] The XRD pattern for MgCuPO$_4$ indicated almost similar diffraction patterns to Mg$_3$(PO$_4$)$_2$ and Cu$_3$(PO$_4$)$_2$. The width of these spikes was evidence of the amorphous nature of MgCuPO$_4$. The incorporation of Ag$_3$PO$_4$ is indicated in Fig. 2(b). Three different XRD patterns for S$_1$, S$_2$, and S$_3$ are represented in Fig. 2(b). There were multiple reflections associated with S$_1$, S$_2$, and S$_3$. The XRD pattern shows the crystalline nature of Ag$_3$PO$_4$. The strong peaks for Ag$_3$PO$_4$ at $2\theta = 29.1°$, $33.3°$, $36.6°$,

47.5°, 52.1°, 55.0°, and 57.5° correspond to the (200), (210), (211), (310), (222), (320), and (321) planes. This XRD pattern correlated with JCPDS 06-0505, which shows the formation of Ag$_3$PO$_4$.[21] As the amount of MgCuPO$_4$ decreased, the intensity of XRD spikes for Ag$_3$PO$_4$ increased. The lack of a positional shift in the Ag$_3$PO$_4$ peaks indicates that Ag$_3$PO$_4$ was not incorporated into the MgCuPO$_4$ lattice, but rather developed on the MgCuPO$_4$ surface.[22] Table 2 shows the lattice parameters of the samples.

The specific surface areas (SSAs) of MgCuPO$_4$ and the MgCuPO$_4$–Ag$_3$PO$_4$ (S$_2$) nanocomposite were calculated using the Brunauer–Emmett–Teller (BET) technique, because S$_2$ demonstrated the best performance compared to S$_1$ and S$_3$, as described in the following part. The N$_2$ adsorption–desorption isotherms of MgCuPO$_4$ and S$_2$ are shown in Fig. 2(c) and (d). The BET graphs for MgCuPO$_4$ and S$_2$ exhibit an IV-type hysteresis loop, showing their porous structure. The porous behavior of MgCuPO$_4$ and S$_2$ resulted in decreases in electrolyte ion diffusion time. The SSA of MgCuPO$_4$ and S$_2$ were 15.72 and 19.34 m^2 g^{-1}, respectively. The total pore volumes for MgCuPO$_4$ and S$_2$ estimated through BET calculations were 0.04928 and 0.052596 cm^3 g^{-1}, respectively. The smaller SSA and pore volume of MgCuPO$_4$ compared to S$_2$ were due to the absence of Ag$_3$PO$_4$ in the MgCuPO$_4$–Ag$_3$PO$_4$ nanocomposite. Furthermore, this may be due to the distribution of Ag$_3$PO$_4$ NPs into MgCuPO$_4$.[23]

Fig. 3(a) and (b) show the FTIR spectra of amorphous MgCuPO$_4$, S$_1$, S$_2$, and S$_3$. The band for the O–P–O bond (ν_4 PO$_4^{3-}$) for the triply degenerate asymmetric mode occurred at 563 cm^{-1}. While the band at 1036 cm^{-1} belongs to the P–O bond (ν_3 PO$_4^{3-}$) stretching mode. The above-mentioned bands are evidence of the presence of phosphate (PO$_4^{3-}$). The bands moved to a lower wavenumber as the amount of Ag$_3$PO$_4$ increased in the MgCuPO$_4$–Ag$_3$PO$_4$ nanocomposites.[24] The band appearing at 1645 cm^{-1} belongs to ν_1 (A$_1$) H$_2$O and those at 3200–3800 cm^{-1} belong to ν_2 (A$_1$) H$_2$O. After the incorporation of Ag$_3$PO$_4$ (S$_1$, S$_2$, and S$_3$), the band intensities rose considerably, showing that the percentages of phosphorous and water on the MgCuPO$_4$–Ag$_3$PO$_4$ surface increased.[25] The adsorbed water resulted in increased storage performance due to an enhanced inter-particle path.[26,27]

3.1.3. Optical properties of MgCuPO$_4$–AgPO$_4$.
UV-vis absorption spectroscopy was applied to check the impact of Ag$_3$PO$_4$ on the optical performance of MgCuPO$_4$. The spectra are shown in Fig. 3(c). In a deformed octahedral coordinated environment, MgCuPO$_4$ has an absorption edge at 808 nm and a second absorption edge at 1000 nm, which are due to Cu$^+$ and Mg$^+$, respectively.[28,29] Because of the decreasing fractions of MgCuPO$_4$ found in MgCuPO$_4$–Ag$_3$PO$_4$ nanocomposites, the absorptivity of MgCuPO$_4$ progressively declines from S$_1$ to S$_3$. Furthermore, as the proportions of MgCuPO$_4$ decreased, the absorption edge red shifted towards the visible region. The existence of more Ag$_3$PO$_4$ NPs than MgCuPO$_4$, which absorbs in the visible region, causes the peaks to redshift. This redshift may also be due to narrowing of the band gap, as evidenced by the altered Kubelka–Munk function of light energy ($\alpha h \nu$)^2 versus photon energy ($h\nu$), as shown in Fig. 3(d). The Tauc equation
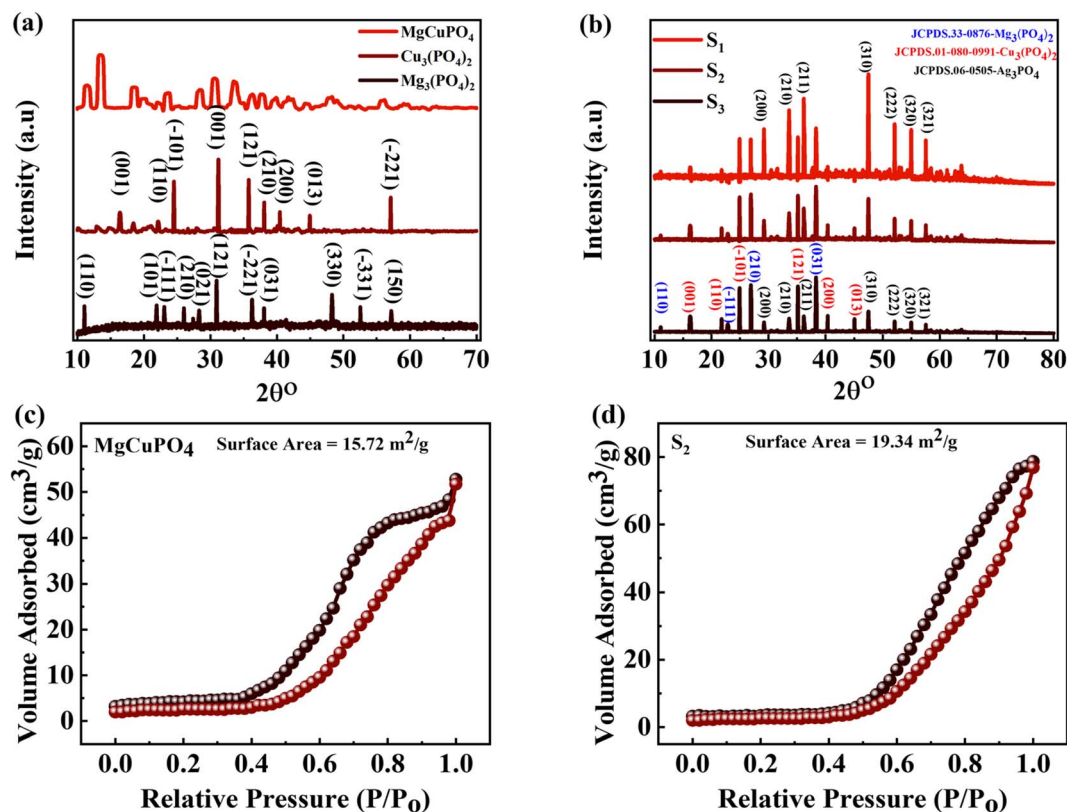
Fig. 2 (a) The XRD pattern for $Mg_3(PO_4)$, $Cu_3(PO_4)$, and $MgCuPO_4$. (b) The XRD pattern for $MgCuPO_4–Ag_3PO_4$ (S_1, S_2, S_3) nanocomposites. (c and d) BET measurement for $MgCuPO_4$ and the S_2 nanocomposite.

was used to determine the band gap (E_g) values of the samples.[30,31]

$$(\alpha h \nu)^2 = K(h \nu - E_g) \qquad (7)$$

The absorption coefficient is denoted by α and the proportionality constant by K. K was determined from $K = (2.303 \times 10^3)(A)/L$, where absorbance is represented by A and optical path by L (1 cm). The E_g value was estimated by extrapolating the straight line of the image shown in Fig. 3(d). E_g values for S_1, S_2, and S_3 and amorphous $MgCuPO_4$ were 3.9, 3.6, 3.5, and 4.3 eV, respectively. The electrical insulating properties of amorphous $MgCuPO_4$ were reflected in its high E_g value. The gradual drop in E_g in $MgCuPO_4–AgPO_4$ nanocomposites was due to the combined impact between the two elements. The overlapping of energy levels causes a reduction in the band gap according to

energy band theory. This indicates that Ag_3PO_4 were well developed on the $MgCuPO_4$ surface, exhibiting the combined electronic characteristics.[32,33]

3.1.4. XPS spectrum for $MgCuPO_4–AgPO_4$. Because of the dispersion of Ag_3PO_4 NPs on the $MgCuPO_4$ surface, XPS was used to analyze the surface composition of $MgCuPO_4$ and $MgCuPO_4–AgPO_4$ nanocomposites. The XPS spectrum of S_2 showed the presence of several distinct peaks due to Mg, P, C 1s, Ag, O 1s, and Cu, as indicated in Fig. 4(a). Fig. 4(b) depicts the deconvoluted core level spectrum of Mg 2p, which includes two bands at 49 and 51 eV binding energy corresponding to Mg^{2+} and Mg^0, respectively.[34] The XPS spike for Cu $2p_{3/2}$ located at 932.5 eV correlates to Cu^{2+} possibly reacting with a phosphate ion. The peak for Cu $2p_{1/2}$ appeared at 952.5 eV, as indicated in Fig. 4(c).[35] The XPS spectrum for P 2p is represented in Fig. 4(d).

Table 2 Structural parameters for the analysis of $MgCuPO_4$ and $MgCuPO_4–Ag_3PO_4$ nanocomposites

	Lattice parameters			Volume ($nm)^3$	Particle size (nm)	Strain (ε_r) (10^{-3})	Density (g cm^{-3})	Dislocation density $(10^{15} m^{-2})$
Sample	α	β	Γ					
Standard	7.599	8.235	5.076					
$MgCuPO_4$	7.597	8.237	5.075	0.38	40–50	0.65	5.4087	0.55
S_1	7.600	8.240	5.075	0.41	51–56	0.71	5.4093	0.58
S_2	7.613	8.243	5.074	0.43	53–58	0.69	5.4098	0.63
S_3	7.615	8.247	5.074	0.44	52–59	0.70	5.4100	0.71
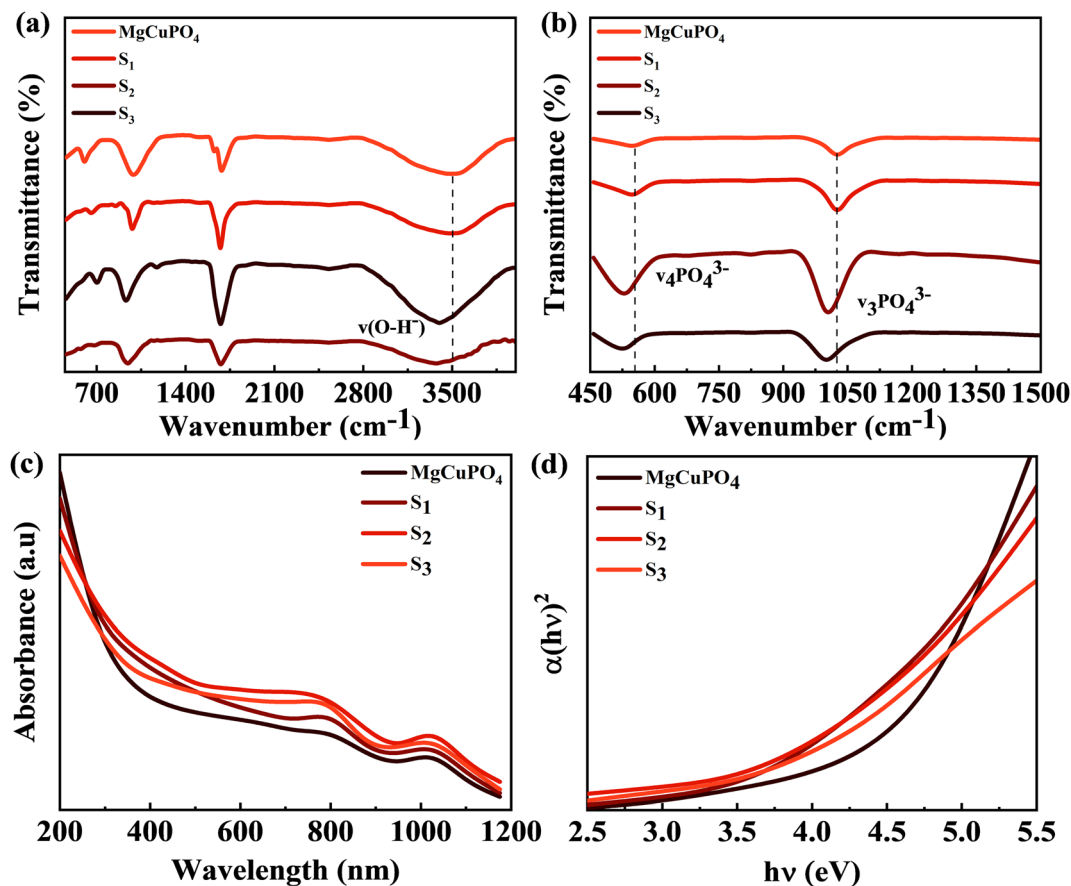
Fig. 3 (a) FTIR spectra for MgCuPO$_4$, S$_1$, S$_2$, and S$_3$ at 500–4000 cm^{-1}. (b) FTIR spectra for MgCuPO$_4$, S$_1$, S$_2$, and S$_3$ at 450–1500 cm^{-1}. (c) UV-vis spectra for MgCuPO$_4$, S$_1$, S$_2$, and S$_3$. (d) The band gap determination for MgCuPO$_4$, S$_1$, S$_2$, and S$_3$.

The presence of P 2p$_{1/2}$ at 135 eV and P 2p$_{3/2}$ at 133 eV confirm the presence of phosphorous. The deconvoluted XPS spectrum of P 2p showed that the first peak at 133 eV accounts for 75–80% of the P 2p signal. This can be ascribed to the oxidation of the MgCuPO$_4$ surface metal phosphate molecule in PO$_4{}^{3-}$.[36] The second spike at 135 eV showed the presence of 10–20% residual metaphosphate.[37] S$_2$ demonstrated the presence of symmetrical spin–orbit components. The XPS spectra for Ag showed two distinct peaks which were separated by 6 eV. The Ag 3d$_{5/2}$ peak appeared at 368 eV and Ag 3d$_{3/2}$ peak appeared at 374 eV, which corresponds to Ag$^+$, as indicated in Fig. 4(e).[38]

3.1.5. Morphological study of MgCuPO$_4$–AgPO$_4$. SEM analysis was used to examine the shape of MgCuPO$_4$ and its three composites with Ag$_3$PO$_4$ (S$_1$, S$_2$, and S$_3$). Fig. 5(a)–(d) depict an uneven form of amorphous MgCuPO$_4$ and its composites with Ag$_3$PO$_4$ with 40–50 nm particle size. Fig. 5 shows that as the amorphous MgCuPO$_4$ content of the nanocomposite decreased, more Ag$_3$PO$_4$ NPs were found on the surface of the amorphous MgCuPO$_4$. However, for S$_1$ and S$_3$, the recombination of ions could restrict the diffusion of ions. The recombination of ions could be attributed to an over-abundance of Ag$_3$PO$_4$, which restricts the movement of MgCuPO$_4$ ions.[39,40]

3.2. Electrochemical results

The synthesized samples (MgCuPO$_4$, S$_1$, S$_2$, and S$_3$) were then electrochemically tested using CV measurements, which were determined in the potential window (PW) of 0–0.6 V at a scan rate of 3–50 mV s^{-1}, as depicted in Fig. 6. For all samples, faradaic behavior was observed from the presence of redox peaks. This was because of the faster movement of ions within the materials, causing a redox reaction at the surface of the electrodes.[41,42] S$_2$ had the greatest redox current strength at 3 mV s^{-1} scan rate compared to the other MgCuPO$_4$–AgPO$_4$ nanocomposites. This shows that the addition of Ag$_3$PO$_4$ increased the redox current due to the synergetic impact of MgCuPO$_4$ and Ag$_3$PO$_4$. But further addition of Ag$_3$PO$_4$ influenced the redox potentials, as can be seen from the CV plot of S$_3$ (Fig. 6(d)). The finding suggested that electrolyte ions engage extensively with the numerous electro-active sites of the materials when the amount of Ag$_3$PO$_4$ increases. With higher loadings of Ag$_3$PO$_4$ in MgCuPO$_4$, the electrical transmission route and electrolyte ion diffusion rate of the nanocomposites differ. This indicated that the number of phosphate groups in the MgCuPO$_4$–Ag$_3$PO$_4$ composite, as well as metal ion concentrations, affect electron and ion motion.[43] Furthermore, the variations in anodic and cathodic potentials can be linked to the
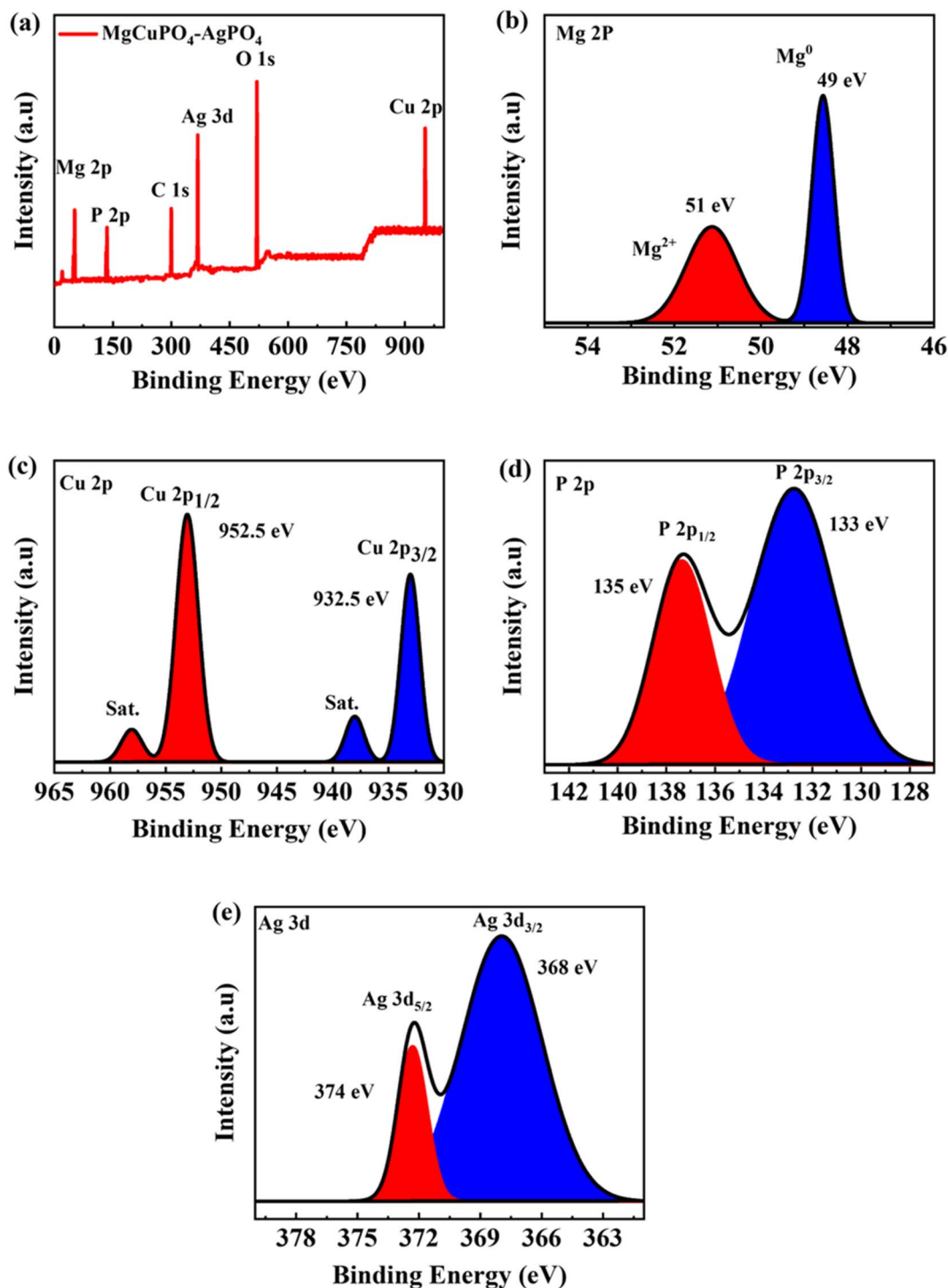
Fig. 4 (a) XPS survey spectrum for S$_2$. (b) XPS spectrum for Mg. (c) XPS spectrum for Cu 2p. (d) XPS spectrum for P 2p. (e) XPS spectrum for Ag 3d.

presence of the redox process.[44] The CV curve of MgCuPO$_4$ changes its shape at 100 mV s^{-1} (Fig. 6(a)) because the electrolyte ions did not reach the MgCuPO$_4$ inner sites.[45] S$_2$ had a greater CV area (and thus a greater specific capacity) than MgCuPO$_4$ at a low scan rate. S$_2$ also maintained its form at higher scan rates due to its stable behavior.[46,47] Fig. 6(a)–(d) illustrate the CV curves for S$_2$ and the other samples (MgCuPO$_4$,

S$_1$, and S$_3$) that were gradually enhanced with rising scan rates (3–50 mV s^{-1}). Fig. S1† shows the CV curves for MgCuPO$_4$, S$_1$, and S$_3$ at an operating potential of 0–0.8 V.

For battery-type materials, the most suitable word to determine the storage capability is the specific capacity (C g^{-1}). However, some researchers in the literature also use capacitance (F g^{-1}) which is not correct. Table 3 shows the values of
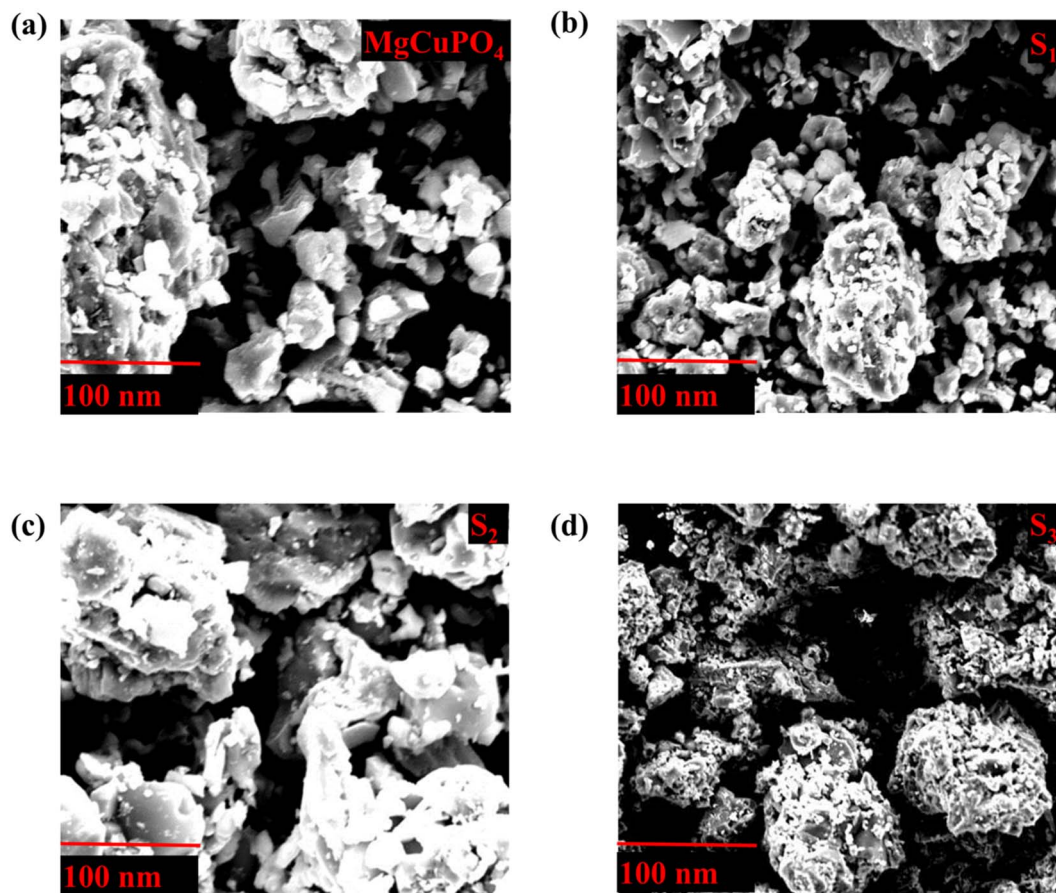
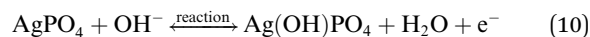Fig. 5 (a–d) SEM images for S_1, S_2, S_3, and S_4 composites.

specific capacity at all scan rates. Eqn (8) can be used to determine the specific capacity.[48]

$$Q_s = \frac{1}{m\Delta v} \int_{V_i}^{V_f} I \times V \mathrm{d}V \tag{8}$$

In eqn (8), Q_s indicates the specific capacity, m is the active mass, Δv represents the change in scan rate; the current is denoted by I, and the operating potential by V. The specific capacities calculated for $MgCuPO_4$, S_1, S_2, and S_3 at various scans are represented in Fig. 7(a). The specific capacities for $MgCuPO_4$–Ag_3PO_4 nanocomposites were higher than that for $MgCuPO_4$. The specific capacity for S_2 at 3 mV s^{-1} was 839 C g^{-1}, which was higher than that for $MgCuPO_4$ (335 C g^{-1}), S_1 (442 C g^{-1}), or S_3 (671 C g^{-1}). The specific capacities for all samples ($MgCuPO_4$, S_1, S_2, and S_3) at 3 mV s^{-1} are represented in Fig. 7(b). When an amount of Ag_3PO_4 is added into the heterostructure of $MgCuPO_4$, the specific capacity increases due to the combined impact of $MgCuPO_4$–Ag_3PO_4, with a large number of accessible pores and faster movement of ions. A further increase in the amount of Ag_3PO_4 resulted in a decrease in its capacity. An excess amount of Ag_3PO_4 also results in blockage of a number of pores. Therefore, the specific capacity for S_3 decreases.

The positive and negative current spikes measured through CV readings of S_2 gradually increased with the square root of the

scan rate. The value of the I_{pa}/I_{pc} fraction was almost 1. This indicated that the reversible faradaic processes were responsible for charge storage, as shown in Fig. 7(c).[49] The linear relation between anodic and cathodic currents was evidence of the battery nature of the $MgCuPO_4$–Ag_3PO_4 (S_2) nanocomposite. Fig. 7(d) indicates a straight-line relationship between voltage and log of scan rate, which proves the diffusion-controlled process for S_2. The chemical equations below can be used to describe redox reactions.[50]

$$MgCuPO_4 + OH^- \xleftrightarrow{\text{reaction}} MgCu(OH)PO_4 + H_2O + e^- \tag{9}$$

$$AgPO_4 + OH^- \xleftrightarrow{\text{reaction}} Ag(OH)PO_4 + H_2O + e^- \tag{10}$$

The discharge profiles of $MgCuPO_4$ and $MgCuPO_4$–Ag_3PO_4 nanocomposites obtained using the GCD method are shown in Fig. 8(a)–(d). The shape of the GCD curves was non-linear for $MgCuPO_4$, S_1, S_2, and S_3 because of deep ion interaction, showing that charge storage contribution comes mainly from the redox reactions. At a current density of 2 A g^{-1}, S_2 had the greatest discharge time compared to the other $MgCuPO_4$–$AgPO_4$ nanocomposite electrodes. At 3.2 A g^{-1} current, the GCD trajectory of $MgCuPO_4$ was also relatively shorter than that of S_2. This showed that the performance of $MgCuPO_4$ decreases with current density more frequently than the other $MgCuPO_4$–
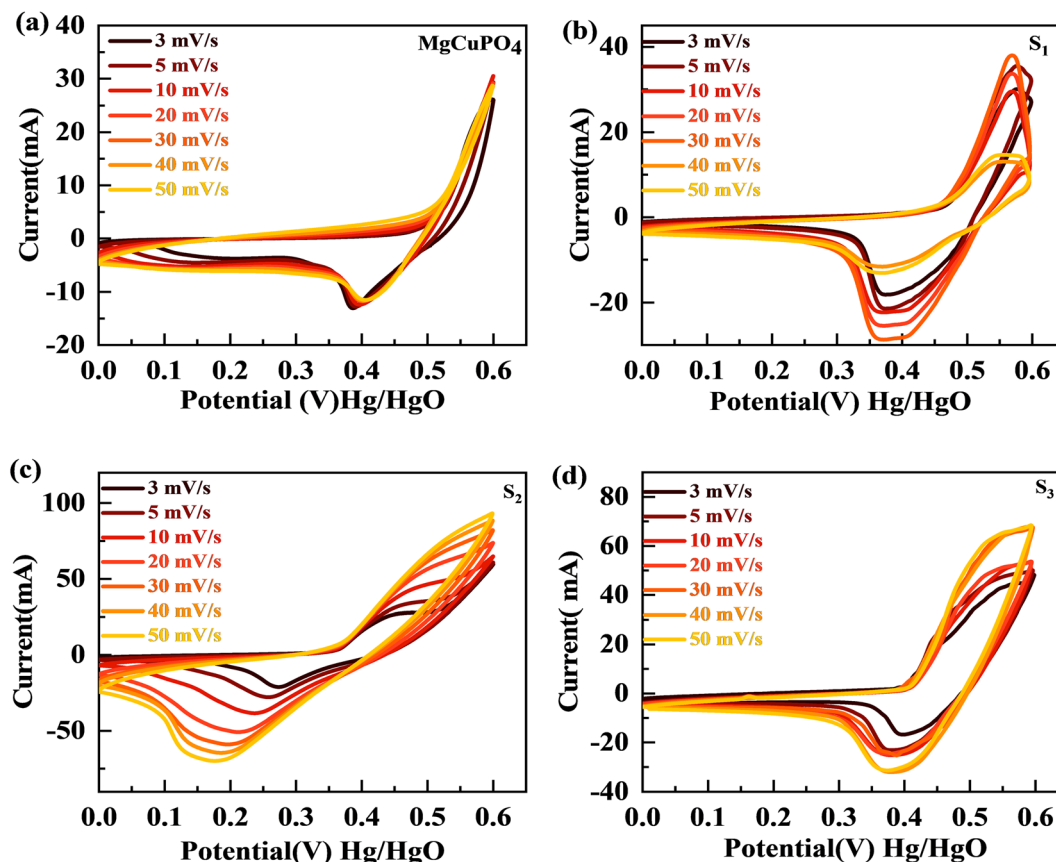
Fig. 6 (a–d) The CV curves for MgCuPO$_4$, S$_1$, S$_2$, and S$_3$, respectively.

Ag$_3$PO$_4$ nanocomposites, as illustrated by Fig. 8(a)–(d). The GCD comparison at 2.0 A g^{-1} for MgCuPO$_4$, S$_1$, S$_2$, and S$_3$ is represented in Fig. 9(a). As can be seen from Fig. 9(a), S$_2$ had the largest plateau region compared to the other samples. This may be due to the larger surface area exposed to electrolytic ions, faster transportation of ions, and higher conductivity of S$_2$. The specific capacity, Q_s, of the electrodes was determined using eqn (11) from the galvanostatic discharge data.

$$Q_s = \frac{I \times \Delta t}{m} \tag{11}$$

in eqn (11), Q_s represents the specific capacity, I is the current, Δt indicates the discharge time, and m is the active mass. Fig. 9(b) depicts a plot of specific capacity for MgCuPO$_4$, S$_1$, S$_2$, and S$_3$ against current density derived from the GCD curves. At all present current densities, the specific capacity for MgCuPO$_4$ had reduced from 316 (2 A g^{-1}) to 169 C g^{-1} (3.2 A g^{-1}), with 53% capacity retention. S$_1$ had a capacity retention of 58% with a capacity of 330 C g^{-1} at 2 A g^{-1} and 192 C g^{-1} at 3.2 A g^{-1}. Again S$_2$ outperforms the other composite materials, showing 1138 C g^{-1} capacity at 2 A g^{-1}. S$_2$ can retain 663.8 C g^{-1} capacity at 3.2 C g^{-1} showing 59% capacity retention. Furthermore, an

Table 3 Specific capacity for MgCuPO$_4$, S$_1$, S$_2$, and S$_3$ through CV and GCD

Scan rate (mV s^{-1})	Specific capacity (C g^{-1})							
	MgCuPO$_4$		S$_1$		S$_2$		S$_3$	
	CV	GCD	CV	GCD	CV	GCD	CV	GCD
3	336.16	317	442	330	839	1138	671	512
5	264.60	269	379.71	269	682.04	933	583.42	478
10	200.12	245	305.08	251	571.73	891	447.96	447
20	129.15	215	212.86	236	333.16	832	257.97	426
30	71.05	192	122.49	225	194.76	745	184.12	398
40	40.49	183	83.07	210	126.813	682	119.18	355
50	20.88285	169	49.40	192	86.44	663	70.54	313
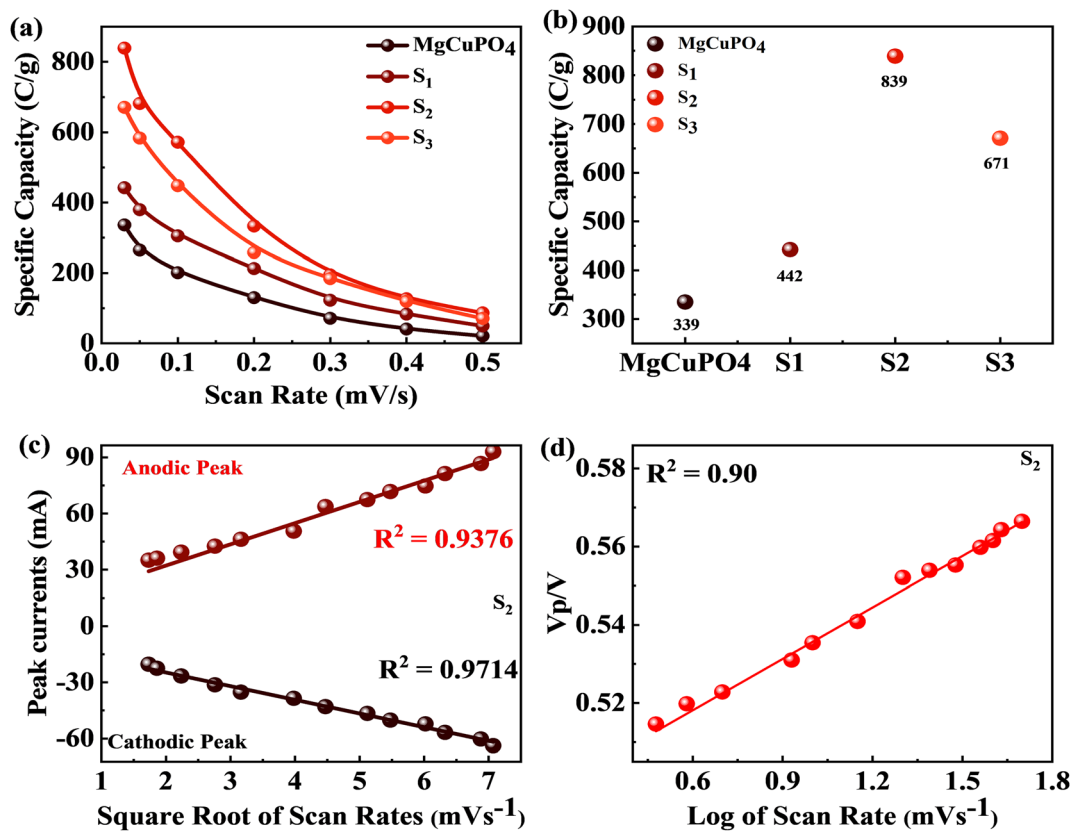
Fig. 7 (a) Specific capacity for MgCuPO$_4$, S$_1$, S$_2$, and S$_3$ at various scan rates. (b) Specific capacity for MgCuPO$_4$, S$_1$, S$_2$, and S$_3$ at 3 mV s^{-1} scan rate. (c) Anodic and cathodic peaks calculated for S$_2$. (d) Peak voltage plotted against log of scan rate for S$_2$.

increase in the wt% ratio of Ag$_3$PO$_4$ decreases the overall performance. The specific capacities decrease for S$_3$ to 512 C g^{-1} at 2 A g^{-1} and 313.6 C g^{-1} at 3.2 A g^{-1}, demonstrating 61% capacity retention.

This increase in rate capacity was due to the presence of Ag$_3$PO$_4$ NPs, which decreased the internal impedance of MgCuPO$_4$.[51] Among all the MgCuPO$_4$–Ag$_3$PO$_4$ (S$_1$, S$_2$, and S$_3$) nanocomposites studied, S$_2$ had the highest capacity. The increased electrochemical performance for S$_2$ was due to two conflicting effects: raising the quantity of Ag$_3$PO$_4$ increases the conductivity of MgCuPO$_4$–Ag$_3$PO$_4$ nanocomposites. However, too many Ag$_3$PO$_4$ nanoparticles degrade the performance of the S$_3$ electrode due to agglomerations produced, which reduces the contact area between the electrode and electrolytic solution. Another cause was the lack of amorphous MgCuPO$_4$ in S$_3$, as amorphous MgCuPO$_4$ was responsible for increased active sites for redox reactions.[52] Therefore, owing to the structural stability of crystalline Ag$_3$PO$_4$ NPs, the rate capacity of S$_2$ remains greater than that of MgCuPO$_4$. Fig. 9(c) indicates the comparative calculated specific capacities for MgCuPO$_4$, S$_1$, S$_2$, and S$_3$ at 2.0 A g^{-1}.

The electrochemical impedance spectra (EIS) of the electrode materials were measured to determine charge and ion transport. The Nyquist graphs of amorphous MgCuPO$_4$, S$_1$, S$_2$, and S$_3$ are shown in Fig. 9(d). Because of the roughness of the electrode surface, uneven electric field, and varying electrochemical

activity, the form of the EIS plots departs from the semicircular shape.[53] The corresponding series resistance was calculated using the contact of the EIS graphs with the real part of the impedance spectrum. At high frequencies, the semicircle width is attributed to charge transfer impedance (R_{ct}).[54] In Fig. 9(d) (inset), the circuit diagram for the fitted Nyquist plot is also represented. The semicircle can be seen from the ZCPE and R_{ct} parallel connection in the circuit diagram. According to the EIS diagram, the R_s values for S$_1$, S$_2$, S$_3$, and MgCuPO$_4$ were 0.72, 0.65, 0.81, and 1.05 U, respectively, as shown in Fig. 9(d). The lower R_s values of all MgCuPO$_4$–AgPO$_4$ nanocomposites compared to amorphous MgCuPO$_4$ nanocomposites suggest higher conductance. Moreover, the semicircle diameter of MgCuPO$_4$ was considerably bigger than that of the MgCuPO$_4$–AgPO$_4$ nanocomposites in the Nyquist plots, which results in greater charge transfer resistance. In all the MgCuPO$_4$–Ag$_3$PO$_4$ nanocomposites studied, S$_2$ had the shortest diameter, indicating the lowest internal resistance. Furthermore, the straight line for S$_2$ was the sharpest, indicating the lowest ion diffusion resistance. The high-resolution EIS spectra for MgCuPO$_4$, S$_1$, S$_2$, and S$_3$ are represented in Fig. 9(e). A potential-dependent capacity test was used to further explore the effect of Ag$_3$PO$_4$ modification on the electrical characteristics of MgCuPO$_4$. MS plots were made from the capacitances obtained from the imaginary portion of the impedance. Fig. 9(f) depicts the MS plots for MgCuPO$_4$, S$_1$, S$_2$, and S$_3$. The dominant charge carriers
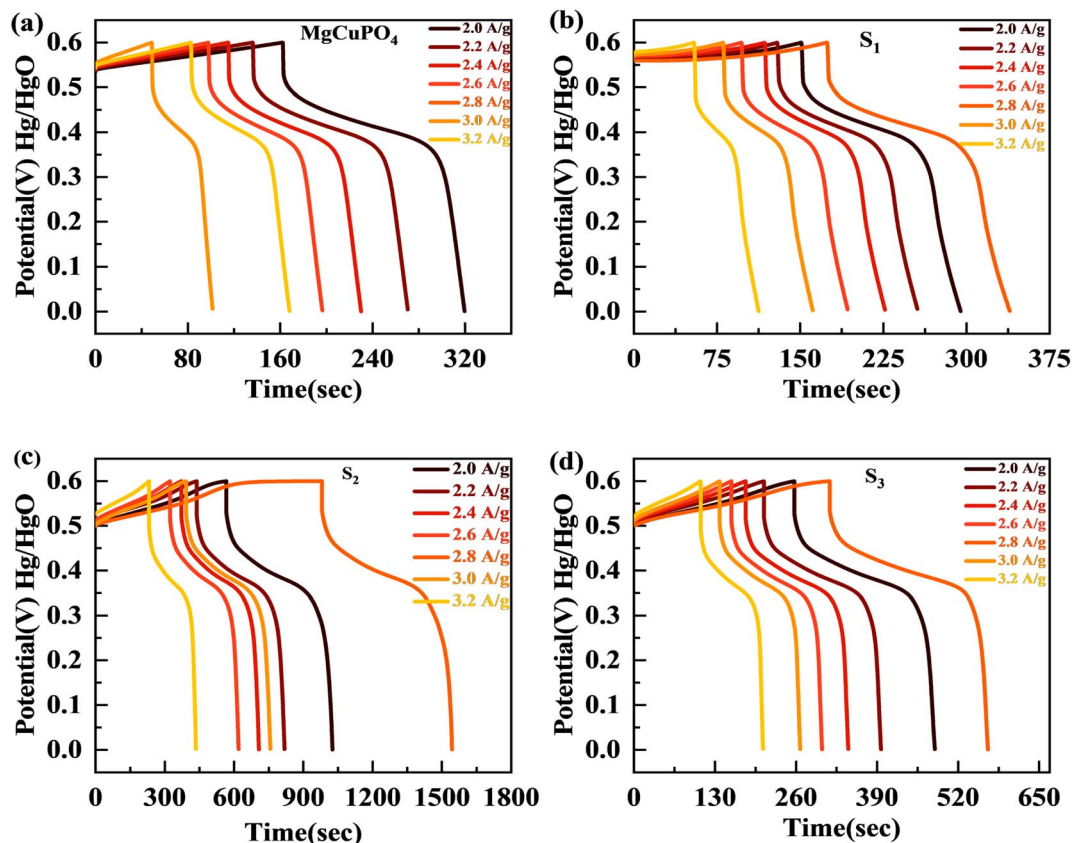
Fig. 8 (a–d) The GCD plots for MgCuPO$_4$, S$_1$, S$_2$, and S$_3$ at different currents.
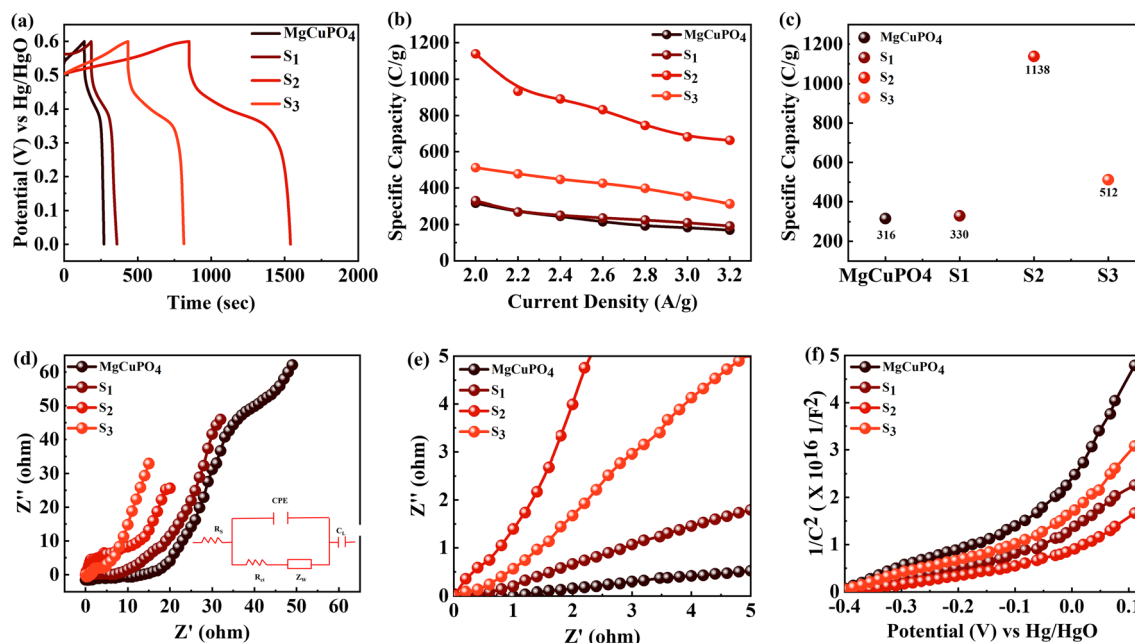

Fig. 9 (a) GCD comparison for MgCuPO$_4$, S$_1$, S$_2$, and S$_3$ at 2.0 A g^{-1} current density. (b) Specific capacity computed for MgCuPO$_4$, S$_1$, S$_2$, and S$_3$ at varied current densities. (c) Specific capacity computed for MgCuPO$_4$, S$_1$, S$_2$, and S$_3$ at 2 A g^{-1} current density. (d) EIS graph for MgCuPO$_4$, S$_1$, S$_2$, and S$_3$. (e) High-magnification EIS images for MgCuPO$_4$, S$_1$, S$_2$, and S$_3$. (f) MS plot for MgCuPO$_4$, S$_1$, S$_2$, and S$_3$.

in all MgCuPO$_4$, S$_1$, S$_2$, and S$_3$ materials were electrons, as indicated by the positive slope of the straight lines (n-type semiconductors). The slope obtained from the straight line plotted between $1/C^2$ and V can be used to evaluate charge carrier density among electrode materials. The charge carrier has a negative relationship with the MS inclination.[55] The S$_1$, S$_2$, and S$_3$ slopes were lower than those of MgCuPO$_4$, implying that the MgCuPO$_4$–Ag$_3$PO$_4$ composites had a greater charge carrier density. The S$_2$ curve had the lowest slope, demonstrating its increased electron density. These findings suggest that the incorporation of Ag$_3$PO$_4$ into MgCuPO$_4$ results in a higher density of charge carriers.[56]

The electron transmission rate of crystalline Ag$_3$PO$_4$ NPs differs from that of diffuse MgCuPO$_4$. The number of pores provided by MgCuPO$_4$ was used to store the electrolyte ions that were able to penetrate the inner surface of MgCuPO$_4$. Most of the amorphous MgCuPO$_4$ surfaces were engaged in the faradaic reactions. Additionally, the electrolyte could not reach internal surfaces at a higher scan rate/current density, thus producing a low specific capacity.[57] In contrast, the electrolytic ions interact with the topmost surface layer of Ag$_3$PO$_4$ NPs as well as the inner surface of MgCuPO$_4$. Thus, Ag$_3$PO$_4$ adds useful surface area to unutilized amorphous MgCuPO$_4$ surfaces and maintains a large number of oxidation/reduction reactions at

higher currents.[58] Despite the fact that amorphous MgCuPO$_4$ offers a porous structure that helps to store more electrolytic ions, it still had low conductance.[59] In this study, the high electrical conductivity of Ag$_3$PO$_4$ NPs fixed on the weakly conductive amorphous MgCuPO$_4$ accelerates the electron transfer mechanism and lowers the impedance of the MgCuPO$_4$–Ag$_3$PO$_4$ composites. Furthermore, the Ag$_3$PO$_4$ nanoparticles reduce the distance between electron transport routes and the collector, resulting in increased electrochemical performance.[60]

3.3. Supercapattery

The broad PW results in increased energy density for SCs. The supercapattery (S$_2$//AC) was designed with S$_2$ and activated carbon (AC). AC due to its permeable and porous structure allows more electrolyte ions to be stored.[61] The individual CV graphs were originally measured in a three-cell setup for S$_2$ and AC to measure the overall voltage of the supercapattery (Fig. 10(a)). The working PW of AC was 0 to -1 V and that of S$_2$ was 0–0.6 V. Thus, the S$_2$//AC supercapattery was stable over 1.6 V. No redox peak appeared at 0–0.5 V, which showed that the dominant storage mechanism was provided by the capacitive nature of AC. At higher potential, >0.6 V, redox peaks emerged, indicating the faradaic reaction of S$_2$. Fig. 10(b) shows that the
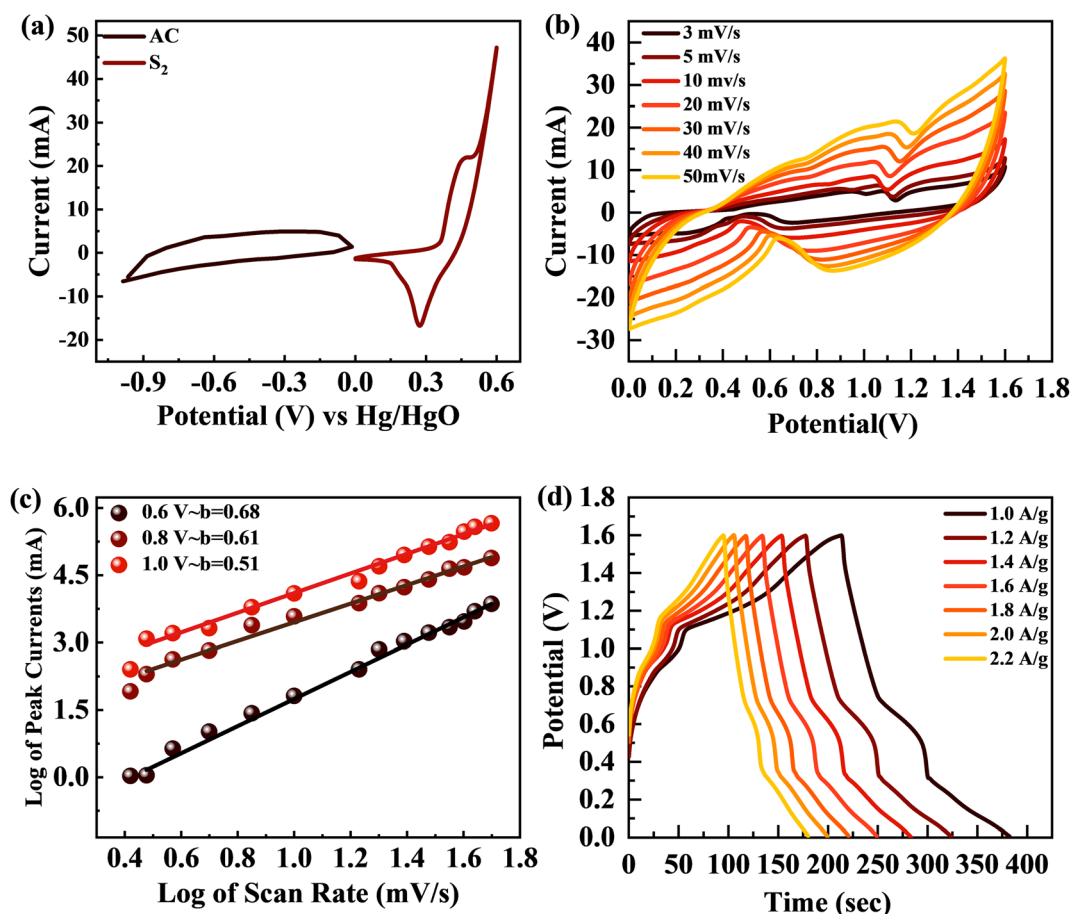

Fig. 10 (a) CV curves for AC and S$_2$ at 3 mV s^{-1}. (b) CV curves for the S$_2$//AC supercapattery at 3–50 mV s^{-1}. (c) *b*-fitting computed for the S$_2$//AC device. (d) GCD curves for the S$_2$//AC supercapattery at 1–2.2 A g^{-1} current density.

shape of the CV graphs for the S_2//AC supercapattery was not altered at a higher scan (100 mV s^{-1}), which proves the high stability of the S_2//AC device.

The power law, which connects current density I with scan rate (v), was used for theoretical study of the electrochemical behavior of the asymmetric device. The charge storage process in a supercapattery is investigated using b-fitting. The b-value was calculated using the slope drawn between the log of scan rate and the log of peak current.

$$I = kv^b \tag{12}$$

$$\ln I = \ln k + b \ln v \tag{13}$$

The adjustable factors are represented by k and b, as stated in the equations, while v is the scan rate and I is the current. The exponent b is critical in deciding the charge accumulation in a supercapattery. For a b-value of 0–0.5, the dominant charge storage process is diffusion regulated. For a b-value of 0.8–1.0, the dominant charge storage process is adsorption/desorption. For a b-value of 0.5–0.8, the storage process is due to both faradaic and adsorption/desorption processes.[62] The b-fitting for this supercapattery (S_2//AC) was between 0.5 and 0.8, as shown in Fig. 10(c). This proves the formation of a supercapattery.

The GCD measurements for the S_2//AC supercapattery were performed at various densities (1.0 to 2.2 A g^{-1}), as depicted in Fig. 10(d). The GCD curves of the S_2//AC device were nearly symmetrical at all currents, which demonstrates its higher stability.[63] Furthermore, the GCD contours were non-linear due to the faradaic response of S_2. The specific capacity for the S_2//AC supercapattery was also calculated from eqn (8) and (11). At a current intensity of 1.0 A g^{-1}, the specific capacity of S_2//AC was 193 C g^{-1}, as indicated in Fig. 11(a). The S_2//AC device can retain 60% of its initial capacity at 2.2 A g^{-1} current. While the capacity through a CV for the S_2//AC supercapattery was 183 C g^{-1} (at 3 mV s^{-1}), as indicated in Fig. 11(b).

Fig. 11(c) and (d) represent the stability test for the S_2//AC supercapattery device against 5000 cycles. The capacity was increased marginally to 110% at the start, owing to the wettability of the electrode surface and slow activation of the electrode.[64] After 5000 cycles, the capacity declined slowly to 92%, showing that the device was stable. The coulombic efficiency after 5000 cycles was retained at 98%. The decay in capacity was due to structural degradation of the electrode materials. The nanocomposite agglomeration as well as separation of the electrode material from the electrolyte are also responsible for the decrease in capacity.[65,66]

Fig. 11(e) depicts the Ragone plot of the estimated energy density (E) and power density (P) of the S_2//AC supercapattery using the following formulae.

$$E \ (\text{W h kg}^{-1}) = \frac{Q\Delta V}{2 \times 3.6} \tag{14}$$

$$P \ (\text{W kg}^{-1}) = \frac{E \times 3600}{\Delta t_d} \tag{15}$$

where Q denotes specific capacity, V denotes the PW, and t_d denotes discharge duration. S_2//AC provided a high energy density as well as an outstanding power density (49.4 W h kg^{-1} at 550 W kg^{-1} and 19.5 W h kg^{-1} at 6382 W kg^{-1}). These results outperformed previous studies, as indicated in Table 4.

4. Oxygen evolution reaction (OER)

Linear sweep voltammetry (LSV) was employed to evaluate the electrocatalytic performance of MgCuPO$_4$, S_1, S_2, S_3, and S_4 composites, as well as the bare stainless steel (SS) substrate. To conduct the investigation, 1 M KOH electrolyte was utilized. The primary objective was to assess their ability to generate a current density of 10 mA cm^{-2} with minimal overpotential, aiming to match the widely employed anode materials RuO$_2$ and IrO$_2$ in various industrial applications. The LSV data revealed distinctive behavior among the tested materials.[67]

$$\eta = E_{\text{RHE}} - 1.23 \ \text{V} \tag{16}$$

The MgCuPO$_4$ composite exhibited an onset overpotential of 340 mV, whereas the S_1 and S_3 composites displayed starting overpotentials of 263 and 221 mV, respectively. In contrast, the S_2 composite showcased an even lower overpotential of 142 mV, further underscoring its electrocatalytic capabilities. Conversely, the bare SS substrate necessitated a higher overpotential of 388 mV to achieve a current density of 10 mA cm^{-2} (Fig. 12(a)).

The bare SS substrate was included in the assessment as a reference point to evaluate the effectiveness of the composites. The higher overpotential required by the bare SS substrate suggests low electrocatalytic activity and inadequate efficiency in the oxygen evolution reaction (OER). Conversely, the significantly lower overpotentials observed for the MgCuPO$_4$, S_1, S_2, and S_3 composites indicate superior performance and potential for diverse applications, particularly in renewable energy conversion and storage devices.

Moreover, Fig. 12(b) illustrates comparable overpotentials at $j = 10$ mA cm^{-2}, a typical measure of OER activity. A lower overpotential implies significantly better performance in the OER.[68,69] These findings highlight the exceptional electrocatalytic capabilities of the MgCuPO$_4$, S_1, S_2 and S_3 composites compared to the bare SS substrate. Their reduced onset overpotentials and improved catalyst utilization suggest the potential to enhance energy storage technologies and enable sustainable energy conversion processes. The effectiveness of the electrochemical processes can be improved by these materials (MgCuPO$_4$, S_1, S_2, and S_3), taking us one step forward to a more environmentally friendly and sustainable energy density.

Tafel plots were used to analyze the reaction kinetics of the MgCuPO$_4$, S_1, S_2, and S_3 materials, as shown in Fig. 12(c). The Tafel slopes reveal information about the reaction response of the materials.
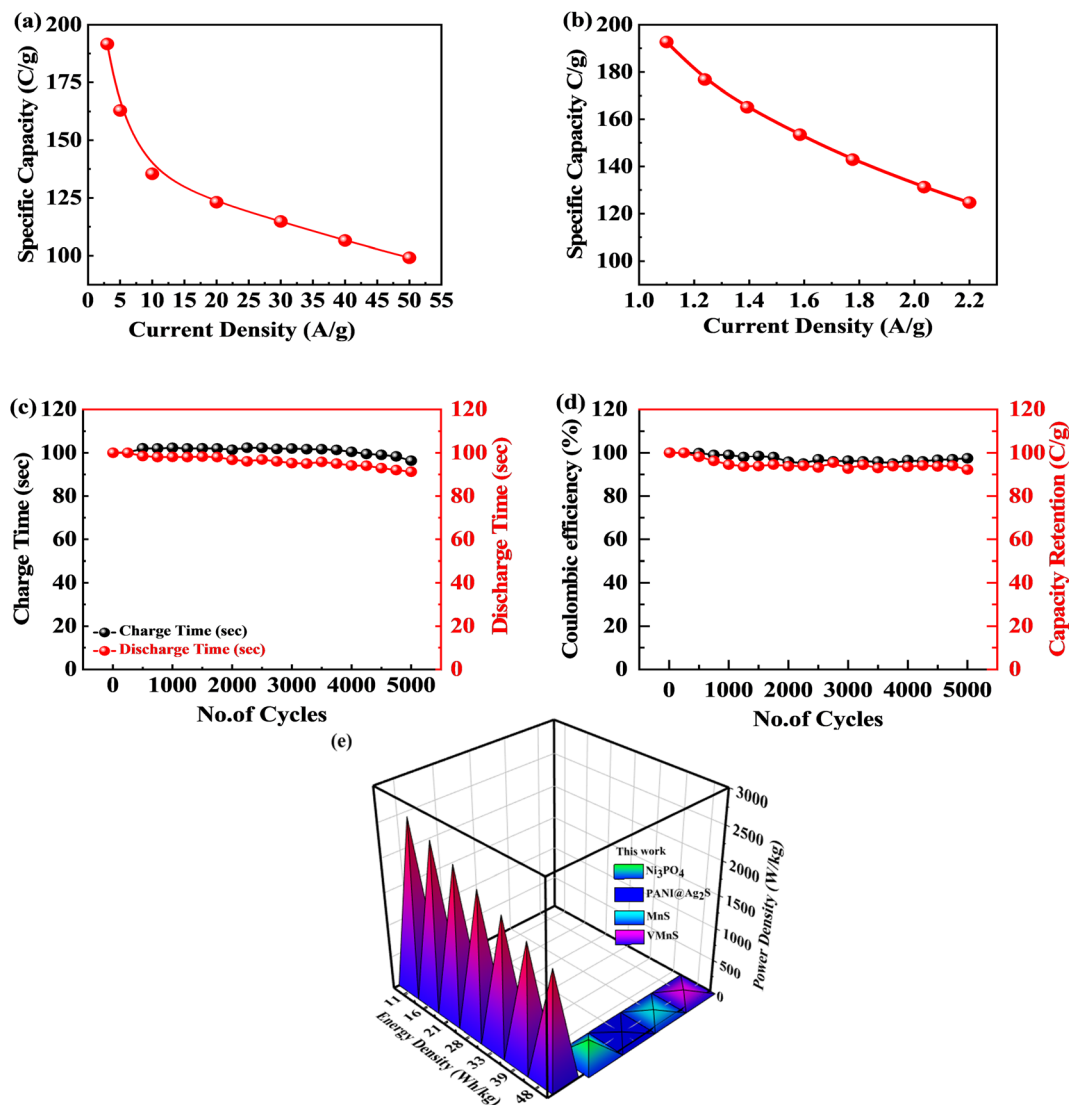
$$\eta = a + b \ln i \tag{17}$$

Fig. 11 (a and b) Specific capacity for the S_2//AC supercapattery computed through CV and GCD. (c and d) Charge/discharge and capacity retention for the S_2//AC supercapattery after 5000 cycles. (e) Energy and power density for the S_2//AC supercapattery.

Table 4 Energy *vs.* power density for the $MgCuPO_4$–Ag_3PO_4//AC device and comparison with the literature

Previous study	Energy density	Power density
Ni–Co–S[70]	42	750
Ni–V–S$_2$ (ref. 71)	12	900
MnS[72]	10.55	294.35
Sr-based materials[73]	21.8	224
Co/WS[74]	42.2	1047
2D VS$_2$/P[75]	28.22	596
MnO$_2$@CoS nanosheets[76]	34	597.24
This work	**49.4**	**550**

The $MgCuPO_4$ composite exhibits a Tafel slope of 103 mV dec^{-1}; the S_1 composite shows a Tafel slope of 95 mV dec^{-1}; S_2 shows a Tafel slope of 49 mV dec^{-1} (see Table 5); and S_3 shows a Tafel slope of 68 mV dec^{-1}. The reduced Tafel slope of S_2

(117 mV dec^{-1}) in comparison to the other composites and bare SS points to quicker reaction rates. As a result, the oxygen evolution process (OER) can occur at greater speeds in the S_2 composite due to its more effective catalytic activity.

The charge transport process inside the $MgCuPO_4$, S_1, S_2, and S_3 materials, along with the bare SS substrate, was examined using electrochemical impedance spectra (EIS), in conjunction with Tafel studies. Significant features were discovered from the Nyquist plots, as illustrated in Fig. 12(d). Surprisingly, the semicircle diameter of the S_2 composite was less than those of the $MgCuPO_4$, S_1, S_2, and S_3 composites. This suggests that the S_2 composite is more conductible. As shown in the insets of Fig. 12(d), analogous circuits were used to analyze the EIS data. These circuits included elements that represented the impedance of the solution (R_s), the inherent resistance (R_1) of the catalyst, and the impedance of the electrocatalytic activity (R_2). Notably, the electrocatalytic resistance of the S_2 composite
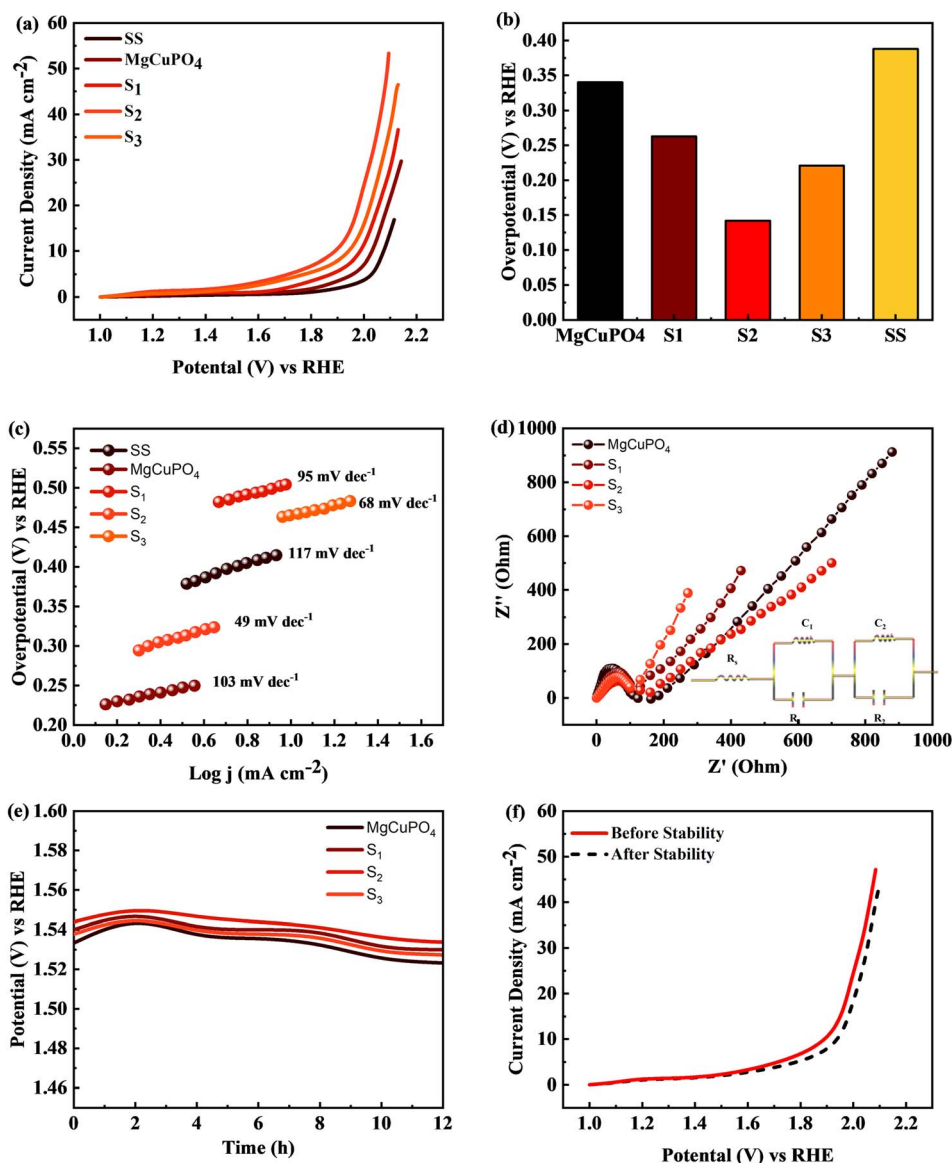
Fig. 12 (a) Linear sweep voltammograms (LSV) of MgCuPO$_4$, S$_1$, S$_2$, and S$_3$ in comparison to SS. (b) Overpotential needed to achieve 10 mA cm^{-2} current for all composites. (c) Tafel plots for SS, MgCuPO$_4$, S$_1$, S$_2$, and S$_3$. (d) EIS measurements for MgCuPO$_4$, S$_1$, S$_2$, and S$_3$ composites. (e) Chronopotentiometric study for MgCuPO$_4$, S$_1$, S$_2$, and S$_3$. (f) Electrocatalytic analysis of S$_2$ composite after OER stability.

Table 5 Comparison of Tafel slope and overpotential of this work with previous studies

Literature	Tafel slope (mV dec^{-1})	Overpotential (mV)	Ref.
Cobalt sulfide thin films	57	300	77
Ni$_{12}$P$_5$ nanocapsule	49.8	152	7
Ni$_x$P$_y$	72.2	157	78
C@Ni–P	64	153	79
MgCuPO$_4$–Ag$_3$PO$_4$ (S$_2$)	**49**	**142**	**This work**

was determined to be 659 Ω cm^2, significantly lower than the resistances of the MgCuPO$_4$ (732 Ω cm^2), S$_1$ composite (788 Ω cm^2) or the S$_3$ composite (914 Ω cm^2). Table S1† presents the

impedance of MgCuPO$_4$, S$_1$, S$_2$, and S$_3$ in the oxygen evolution reaction.

To evaluate the long-term electrochemical stability of the MgCuPO$_4$, S$_1$, S$_2$, and S$_3$ composites, a chronopotentiometric mode was employed. Fig. 12(e) demonstrates a minor potential drop over time, attributed to an improvement in catalytic efficiency. Continuous gas liberation was observed during the stability investigation, indicating the ongoing oxygen evolution process. Fig. 12(f) presents the LSV graphs of S$_2$.

The results of the study indicate that the MgCuPO$_4$, S$_1$, S$_2$, and S$_3$ composites exhibit favorable reaction kinetics and long-term electrochemical stability specifically for the oxygen evolution reaction (OER). The lower Tafel slope observed for the S$_2$ composite suggests faster reaction rates, while the slight reduction in potential during the stability test signifies

improved catalytic efficiency. These characteristics are crucial for ensuring the sustained performance and durability of electrochemical devices, underscoring the significance of these composites in applications related to energy storage and conversion.

5. Conclusions

The sonochemical and hydrothermal technique followed by calcination treatment effectively synthesizes $MgCuPO_4$ and $MgCuPO_4$–Ag_3PO_4 nanocomposites with various $MgCuPO_4$–Ag_3PO_4 content ratios. XRD phase structure analysis verified that the crystalline structure of Ag_3PO_4 NPs increases with decreasing amorphous $MgCuPO_4$ content. The FTIR spectra revealed that phosphate and hydroxyl groups were chemisorbed on the $MgCuPO_4$–Ag_3PO_4 surface. The UV-vis spectroscopic analysis revealed that $MgCuPO_4$–Ag_3PO_4 composites were more conductive than $MgCuPO_4$. The SEM analysis showed that Ag_3PO_4 nanoparticles were firmly fixed on the amorphous surface of $MgCuPO_4$. The $MgCuPO_4$–Ag_3PO_4 nanocomposite-based electrode demonstrated increased rate capability from 53% ($MgCuPO_4$) to 59% at 3.2 A g^{-1}. The rapid electron movement and the large number of active sites given by $MgCuPO_4$ and Ag_3PO_4 composites enhanced the rate capacity. Because amorphous $MgCuPO_4$ has a low electrical conductivity, modifying amorphous $MgCuPO_4$ with crystalline Ag_3PO_4 NPs offers a potential method to increase conductivity and rate capability. The constructed S_2//AC supercapattery had an energy density of 49.4 W h kg^{-1} at 550 W kg^{-1} power density. The S_2//AC supercapattery showed 92% capacity retention after 5000 cycles. Investigation of the OER application demonstrated that S_2 exhibited the lowest Tafel slope, measuring 49 mV dec^{-1}. The results obtained from this study suggest that $MgCuPO_4$–Ag_3PO_4 composites hold great promise as potential candidates for future energy storage devices and further investigation into the oxygen evolution reaction (OER).

Conflicts of interest

There are no conflicts to declare.

Acknowledgements

References

1 M. F. El-Kady, M. Ihns, M. Li, J. Y. Hwang, M. F. Mousavi, L. Chaney, A. T. Lech and R. B. Kaner, *Proc. Natl. Acad. Sci. U. S. A.*, 2015, **112**, 4233–4238.

2 R. Kötz and M. Carlen, *Electrochim. Acta*, 2000, **45**, 2483–2498.

3 F. Larsson and B.-E. Mellander, *J. Electrochem. Soc.*, 2014, **161**, A1611.

4 F. S. Omar, A. Numan, S. Bashir, N. Duraisamy, R. Vikneswaran, Y.-L. Loo, K. Ramesh and S. Ramesh, *Electrochim. Acta*, 2018, **273**, 216–228.

5 G. Z. Chen, *Int. Mater. Rev.*, 2017, **62**, 173–202.

6 A. Numan, N. Duraisamy, F. S. Omar, D. Gopi, K. Ramesh and S. Ramesh, *Prog. Nat. Sci.: Mater. Int.*, 2017, **27**, 416–423.

7 H. Wan, L. Li, Y. Chen, J. Gong, M. Duan, C. Liu, J. Zhang and H. Wang, *Electrochim. Acta*, 2017, **229**, 380–386.

8 X. Lei, S. Ge, Y. Tan, Z. Wang, J. Li, X. Li, G. Hu, X. Zhu, M. Huang and Y. Zhu, *ACS Appl. Mater. Interfaces*, 2020, **12**, 9158–9168.

9 Y. Yang, Y. Zhou, Z. Hu, W. Wang, X. Zhang, L. Qiang and Q. Wang, *J. Alloys Compd.*, 2019, **772**, 683–692.

10 H. Moon, H. Lee, J. Kwon, Y. D. Suh, D. K. Kim, I. Ha, J. Yeo, S. Hong and S. H. Ko, *Sci. Rep.*, 2017, **7**, 41981.

11 L. Tang, F. Duan and M. Chen, *RSC Adv*, 2016, **1244**, 65012–65019.

12 Y. Shao, H. Wang, Q. Zhang and Y. Li, *J. Mater. Chem. C*, 2013, **1**, 1245–1251.

13 D. S. Patil, S. A. Pawar, J. H. Kim, P. S. Patil and J. C. Shin, *Electrochim. Acta*, 2016, **213**, 680–690.

14 D. S. Patil, J. Shaikh, S. Pawar, R. Devan, Y. Ma, A. Moholkar, J. Kim, R. Kalubarme, C. Park and P. Patil, *Phys. Chem. Chem. Phys.*, 2012, **14**, 11886–11895.

15 L. Tang, F. Duan and M. Chen, *J. Mater. Sci.: Mater. Electron.*, 2017, **28**, 7769–7777.

16 B. Pandit, V. Devika and B. R. Sankapal, *J. Alloys Compd.*, 2017, **726**, 1295–1303.

17 K. M. Lee, C. W. Lai, K. S. Ngai and J. C. Juan, *Water Res.*, 2016, **88**, 428–448.

18 H. Hassan, M. W. Iqbal, S. Gouadria, A. M. Afzal and H. Hegazy, *J. Mater. Sci.: Mater. Electron.*, 2023, **34**, 439.

19 R. Mahajan, R. Prakash, S. Kumar, V. Kumar, R. Choudhary and D. Phase, *Optik*, 2021, **225**, 165717.

20 W. Zhao, G. Zhong, M. J. McDonald, Z. Gong, R. Liu, J. Bai, C. Yang, S. Li, W. Zhao and H. Wang, *Nano energy*, 2016, **27**, 420–429.

21 J.-K. Liu, C.-X. Luo, J.-D. Wang, X.-H. Yang and X.-H. Zhong, *CrystEngComm*, 2012, **14**, 8714–8721.

22 R. J. V. Michael, B. Sambandam, T. Muthukumar, M. J. Umapathy and P. T. Manoharan, *Phys. Chem. Chem. Phys.*, 2014, **16**, 8541–8555.

23 Y. Lv, H. Wang, X. Xu, J. Shi, W. Liu and X. Wang, *Chem. Eng. J.*, 2017, **326**, 401–410.

24 P. Benedek, N. Wenzler, M. Yarema and V. C. Wood, *RSC Adv.*, 2017, **7**, 17763–17767.

25 Y. Wang, K. Wang and X. Wang, *J. Colloid Interface Sci.*, 2016, **466**, 178–185.

26 E. Uchaker, Y. Zheng, S. Li, S. Candelaria, S. Hu and G. Cao, *J. Mater. Chem. A*, 2014, **2**, 18208–18214.

27 J. Zheng and C. Huang, *J. New Mater. Electrochem. Syst.*, 2002, **5**, 41–46.

28 V. Stefov, V. Koleva, M. Najdoski, A. Cahil and Z. Abdija, *Maced. J. Chem. Chem. Eng.*, 2020, **39**, 239–249.

29 Z. Hua, B. Li, L. Li, X. Yin, K. Chen and W. Wang, *J. Phys. Chem. C*, 2017, **121**, 60–69.

30 S. Saha, M. Jana, P. Khanra, P. Samanta, H. Koo, N. C. Murmu and T. Kuila, *ACS Appl. Mater. Interfaces*, 2015, **7**, 14211–14222.

31 P. Reunchan, A. Boonchun and N. Umezawa, *Phys. Chem. Chem. Phys.*, 2016, **18**, 23407–23411.

32 S. Saha, M. Jana, P. Khanra, P. Samanta, H. Koo, N. C. Murmu and T. Kuila, *RSC Adv.*, 2016, **6**, 1380–1387.

33 I. W. Hwang, C. Soci, D. Moses, Z. Zhu, D. Waller, R. Gaudiana, C. J. Brabec and A. J. Heeger, *Adv. Mater.*, 2007, **19**, 2307–2312.

34 H.-H. Huang, W.-C. Shih and C.-H. Lai, *Appl. Phys. Lett.*, 2010, **96**, 193505.

35 P. Mondal, A. Sinha, N. Salam, A. S. Roy, N. R. Jana and S. Islam, *RSC Adv.*, 2013, **3**, 5615–5623.

36 B. Wang, J. Liu, Q. Sun, R. Li, T.-K. Sham and X. Sun, *Nanotechnology*, 2014, **25**, 504007.

37 G. Yun, Q. Guan and W. Li, *RSC Adv.*, 2017, **7**, 8677–8687.

38 V. A. Kumar, T. Uchida, T. Mizuki, Y. Nakajima, Y. Katsube, T. Hanajiri and T. Maekawa, *Adv. Nat. Sci.: Nanosci. Nanotechnol.*, 2016, **7**, 015002.

39 C. A. Amarnath, N. Venkatesan, M. Doble and S. N. Sawant, *J. Mater. Chem. B*, 2014, **2**, 5012–5019.

40 S. Nagamuthu, S. Vijayakumar and K.-S. Ryu, *J. Phys. Chem. C*, 2016, **120**, 18963–18970.

41 N. Duraisamy, A. Numan, S. O. Fatin, K. Ramesh and S. Ramesh, *J. Colloid Interface Sci.*, 2016, **471**, 136–144.

42 P. Jaraba, L. Agüı, P. Yanez-Sedeno and J. Pingarron, *Electrochim. Acta*, 1998, **43**, 3555–3565.

43 C. Chen, X. Li, F. Deng and J. Li, *RSC Adv.*, 2016, **6**, 79894–79899.

44 J. Yan, T. Wei, Z. Fan, W. Qian, M. Zhang, X. Shen and F. Wei, *J. Power Sources*, 2010, **195**, 3041–3045.

45 Z. Wu, Y. Lv, Y. Xia, P. A. Webley and D. Zhao, *J. Am. Chem. Soc.*, 2012, **134**, 2236–2245.

46 H. U. Shah, F. Wang, A. M. Toufiq, A. M. Khattak, A. Iqbal, Z. A. Ghazi, S. Ali, X. Li and Z. Wang, *Int. J. Electrochem. Sci.*, 2016, **11**, 8155–8162.

47 A. Numan, N. Duraisamy, F. S. Omar, Y. Mahipal, K. Ramesh and S. Ramesh, *RSC Adv.*, 2016, **6**, 34894–34902.

48 H. u. Hassan, M. W. Iqbal, A. M. Afzal, T. Abbas, A. Zaka, A. Yasmeen, N. A. Noor, S. Aftab and H. Ullah, *Int. J. Energy Res.*, 2022, 1–13.

49 N. Neghmouche and T. Lanez, *Int. Lett. Chem., Phys. Astron.*, 2013, **4**, 37–45.

50 H. Pang, Y.-Z. Zhang, Z. Run, W.-Y. Lai and W. Huang, *Nano Energy*, 2015, **17**, 339–347.

51 R.-Z. Li, R. Peng, K. D. Kihm, S. Bai, D. Bridges, U. Tumuluri, Z. Wu, T. Zhang, G. Compagnini and Z. Feng, *Energy Environ. Sci.*, 2016, **9**, 1458–1467.

52 L. Ma, X. Shen, Z. Ji, G. Zhu and H. Zhou, *Chem. Eng. J.*, 2014, **252**, 95–103.

53 B. Wang, X. He, H. Li, Q. Liu, J. Wang, L. Yu, H. Yan, Z. Li and P. Wang, *J. Mater. Chem. A*, 2014, **2**, 12968–12973.

54 N. Nadiah, F. S. Omar, A. Numan, Y. Mahipal, S. Ramesh and K. Ramesh, *Int. J. Hydrogen Energy*, 2017, **42**, 30683–30690.

55 Z. H. Bakr, Q. Wali, J. Ismail, N. K. Elumalai, A. Uddin and R. Jose, *Electrochim. Acta*, 2018, **263**, 524–532.

56 R. Imani, M. Pazoki, A. Tiwari, G. Boschloo, A. P. Turner, V. Kralj-Iglič and A. Iglič, *Nanoscale*, 2015, **7**, 10438–10448.

57 Z. Gao, X. Wang, J. Chang, D. Wu, L. Wang, X. Liu, F. Xu, Y. Guo and K. Jiang, *RSC Adv.*, 2015, **5**, 48665–48674.

58 S. Vadivel, D. Maruthamani, M. Kumaravel, B. Saravanakumar, B. Paul, S. S. Dhar, K. Saravanakumar and V. Muthuraj, *J. Taibah Univ. Sci.*, 2017, **11**, 661–666.

59 S. Xu, X. Li, Z. Yang, T. Wang, W. Jiang, C. Yang, S. Wang, N. Hu, H. Wei and Y. Zhang, *ACS Appl. Mater. Interfaces*, 2016, **8**, 27868–27876.

60 D. S. Patil, S. A. Pawar, R. S. Devan, M. G. Gang, Y.-R. Ma, J. H. Kim and P. S. Patil, *Electrochim. Acta*, 2013, **105**, 569–577.

61 M. S. Halper and J. C. Ellenbogen, *Supercapacitors: A Brief Overview*, The MITRE Corporation, McLean, Virginia, USA, 2006, p. 34.

62 M. Z. Iqbal, M. M. Faisal, S. R. Ali, S. Farid and A. M. Afzal, *Electrochim. Acta*, 2020, **346**, 136039.

63 Y. Ma, Y. Jia, L. Wang, M. Yang, Y. Bi and Y. Qi, *J. Mater. Chem. A*, 2016, **4**, 10414–10418.

64 G. K. Veerasubramani, K. Krishnamoorthy and S. J. Kim, *J. Power Sources*, 2016, **306**, 378–386.

65 Y. He, W. Chen, X. Li, Z. Zhang, J. Fu, C. Zhao and E. Xie, *ACS Nano*, 2013, **7**, 174–182.

66 R. Kumar, A. Agrawal, R. K. Nagarale and A. Sharma, *J. Phys. Chem. C*, 2016, **120**, 3107–3116.

67 C. Wang, A. Schechter and L. Feng, *Nano Research Energy*, 2023, **2**, e9120056.

68 J. Xu, X. Zhong, X. Wu, Y. Wang and S. Feng, *J. Energy Chem.*, 2022, **71**, 129–140.

69 K. Ham, J. Lee, K. Lee and J. Lee, *J. Energy Chem.*, 2022, **71**, 580–587.

70 J. Cao, Y. Hu, Y. Zhu, H. Cao, M. Fan, C. Huang, K. Shu, M. He and H. C. Chen, *Chem. Eng. J.*, 2021, **405**, 126928.

71 M. Z. Iqbal, M. M. Faisal, S. R. Ali and M. Alzaid, *Solid State Ionics*, 2020, **354**, 115411.

72 S. Kumar, S. Riyajuddin, M. Afshan, S. K. T. Aziz, T. Maruyama and K. Ghosh, *J. Phys. Chem. Lett.*, 2021, **12**, 6574–6581.

73 M. Z. Iqbal, A. Khan, A. Numan, S. S. Haider and J. Iqbal, *Ultrason. Sonochem.*, 2019, **59**, 104736.

74 Y. Wang and N. Herron, *J. Phys. Chem.*, 1987, **91**, 5005–5008.

75 A. Sharma, S. Kapse, A. Verma, S. Bisoyi, G. K. Pradhan, R. Thapa and C. S. Rout, *ACS Appl. Energy Mater.*, 2022, **5**, 10315–10327.

76 Q. Hu, M. Tang, M. He, N. Jiang, C. Xu, D. Lin and Q. Zheng, *J. Power Sources*, 2020, **446**, 227335.

77 S. B. Kale, A. C. Lokhande, R. B. Pujari and C. D. Lokhande, *J. Colloid Interface Sci.*, 2018, **532**, 491–499.

78 J. Li, X. Zhou, Z. Xia, W. Gao, Y. Ma and Y. Qu, *ACS Appl. Mater. Interfaces*, 2016, **8**, 10826–10834.

79 Z. Yu, L. Tetard, L. Zhai and J. Thomas, *Energy Environ. Sci.*, 2015, **8**, 702–730.